LLNL-JRNL-2002387

Lawrence Livermore National Laboratory

Mineralogical and isotopic constraints on early, high-temperature events and reservoirs recorded in the interior of a type B Ca-Al-rich Inclusion from the reduced CV3 chondrite Vigarano

M Liu, J Simon, J Han, L Keller, C Park, N Matsuda

August 2025

Geochimica et Cosmochimica Acta

Disclaimer

This work performed under the auspices of the U.S. Department of Energy by Lawrence Livermore National Laboratory under Contract DE-AC52-07NA27344.

Geochimica et Cosmochimica Acta

Mineralogical and Isotopic Constraints on Early, High-Temperature Events and Reservoirs Recorded in the Interior of a Type B Ca-Al-Rich Inclusion from the Reduced CV3 Chondrite Vigarano

--Manuscript Draft--

Manuscript Number:	GCA-D-25-00121
Article Type:	Article
Keywords:	Calcium-aluminum-rich inclusions, solar nebula, oxygen isotopes, Al-Mg isotope systematic, transmission electron microscopy
Corresponding Author:	JANGMI HAN NASA Johnson Space Center Houston, TX UNITED STATES
Corresponding Author's Institution:	NASA Johnson Space Center
First Author:	JANGMI HAN
Order of Authors:	JANGMI HAN
	Changkun Park
	Ming-Chang Liu
	Nozomi Matsuda
	Justin I. Simon
	Lindsay P. Keller
Abstract:	A coordinated mineralogical and oxygen and Al-Mg isotopic study of a Type B Ca-Al-rich inclusion (CAI) from the reduced CV3 chondrite Vigarano was carried out using transmission electron microscopy and secondary ion mass spectrometry. This CAI, a once molten igneous object, shows heterogeneous oxygen isotopic compositions among its constituent mineral phases. Spinel is uniformly 16O-rich with Δ17O ≤−23‰. The Δ17O values of Al,Ti-diopside in the CAI core range from −11‰ to −18‰, which are positively correlated with its TiO2 contents, whereas diopside in the Wark-Lovering (WL) rim is 16O-rich with Δ17O = −23‰. Melilite in the CAI mantle shows Δ17O values ≤−10‰ only when Åk<15 but becomes more 16O-poor (Δ17O = −3‰ to −9‰) when Åk>15. These correlated chemical and oxygen isotopic variations were likely established during crystallization of melilite and Al,Ti-diopside from a partial melt, while spinel preserves the original 16O-rich composition of the CAI precursor. We infer that a partial melt was isotopically evolving from 16O-rich to 16O-poor during melilite crystallization, then back to 16O-rich during Al,Ti-rich diopside crystallization via exchange with different gas reservoirs of 16O-poor and 16O-rich compositions during heating event(s). Our Al-Mg isotopic measurements of the CAI core and mantle define a single isochron with an inferred initial 26Al/27Al ratio of 4.93×10−5, indistinguishable from that of the WL rim. This indicates that multiple high-temperature events and oxygen isotopic exchange with isotopically distinct gas reservoirs occurred rapidly during the CAI formation.
Suggested Reviewers:	Steve Simon sbs8@unm.edu
	Sasha Krot sasha@higp.hawaii.edu
	Noriko Kita kita@wisc.edu
	Emma Bullock ebullock@carnegiescience.edu
	Jerome Aleon jerome.aleon@mnhn.fr

Dr. Hailiang Dong
Executive Editor
Geochimica et Cosmochimica Acta

February 3, 2025

Dear Dr. Dong

We would like to submit our manuscript entitled **"Mineralogical and Isotopic Constraints on Early, High-Temperature Events and Reservoirs Recorded in the Interior of a Type B Ca-Al-Rich Inclusion from the Reduced CV3 Chondrite Vigarano"** for publication in *Geochimica et Cosmochimica Acta*. In this manuscript, we present the results of coordinated transmission electron microscopy (TEM) and secondary ion mass spectrometry (SIMS) analyses of a Type B Ca-Al-rich inclusion (CAI) to characterize its petrography, mineralogy, chemistry, and oxygen and Al-Mg isotopic compositions. Our TEM observations provide evidence for low degree secondary parent body alteration, which demonstrates that the inclusion retained primary features recorded in the solar nebula and so a great target for studies of the formation and early evolution of the Solar System. Our SIMS oxygen isotope analyses revealed a correlation between oxygen isotopic heterogeneity and CAI mineral chemistry, providing important implications on the isotopic evolution of gas reservoirs in the solar nebula. Finally, our SIMS Al-Mg isotope analyses constrained the timing and timescale for the CAI formation and its oxygen isotopic evolution. Therefore, this manuscript presents studies of fundamental questions regarding the conditions and processes that existed in the early stages of Solar System formation so that we believe that it will be of broad interest to the cosmochemistry community.

We would suggest Audrey Bouvier, Noriko Kita, and Yves Marrocchi as potential Associated Editors.

Thank you for your attention to our manuscript!

Best regards,
Jangmi Han, Ph.D.
Planetary Scientist
Amentum, NASA Johnson Space Center
Email: jangmi.han@nasa.gov

Mineralogical and Isotopic Constraints on Early, High-Temperature Events and Reservoirs Recorded in the Interior of a Type B Ca-Al-Rich Inclusion from the Reduced CV3 Chondrite Vigarano

Jangmi Han [a,b,*], Changkun Park [c,d], Ming-Chang Liu [e,f], Nozomi Matsuda [e], Justin I. Simon [g], and Lindsay P. Keller [g]

[a] Department of Earth and Atmospheric Sciences, University of Houston, Houston, Texas 77204, USA
[b] Amentum, NASA Johnson Space Center, Houston, TX 77058, USA
[c] Division of Glacier and Earth Sciences, Korea Polar Research Institute, Incheon 21990, Republic of Korea
[d] Polar Science, Korea National University of Science and Technology, Daejeon 34113, Republic of Korea
[e] Department of Earth, Planetary, and Space Sciences, UCLA, Los Angeles, CA 90095, USA
[f] Lawrence Livermore National Laboratory, Livermore, CA 94550, USA
[g] Astromaterials Research and Exploration Science, NASA Johnson Space Center, Houston, TX 77058, USA
*Corresponding author. E-mail: jangmi.han@nasa.gov.

Submitted to Geochimica et Cosmochimica Acta, February 3, 2025

Abstract

A coordinated mineralogical and oxygen and Al-Mg isotopic study of a Type B Ca-Al-rich inclusion (CAI) from the reduced CV3 chondrite Vigarano was carried out using transmission electron microscopy and secondary ion mass spectrometry. This CAI, a once molten igneous object, shows heterogeneous oxygen isotopic compositions among its constituent mineral phases. Spinel is uniformly ^{16}O-rich with $\Delta^{17}O \leq -23‰$. The $\Delta^{17}O$ values of Al,Ti-diopside in the CAI core range from −11‰ to −18‰, which are positively correlated with its TiO_2 contents, whereas diopside in the Wark-Lovering (WL) rim is ^{16}O-rich with $\Delta^{17}O = -23‰$. Melilite in the CAI mantle shows $\Delta^{17}O$ values ≤−10‰ only when $Åk_{<15}$ but becomes more ^{16}O-poor ($\Delta^{17}O = -3‰$ to −9‰) when $Åk_{>15}$. These correlated chemical and oxygen isotopic variations were likely established during crystallization of melilite and Al,Ti-diopside from a partial melt, while spinel preserves the original ^{16}O-rich composition of the CAI precursor. We infer that a partial melt was isotopically evolving from ^{16}O-rich to ^{16}O-poor during melilite crystallization, then back to ^{16}O-rich during Al,Ti-rich diopside crystallization via exchange with different gas reservoirs of ^{16}O-poor and ^{16}O-rich compositions during heating event(s). Our Al-Mg isotopic measurements of the CAI core and mantle define a single isochron with an inferred initial $^{26}Al/^{27}Al$ ratio of 4.93×10^{-5}, indistinguishable from that of the WL rim. This indicates that multiple high-temperature events and oxygen isotopic exchange with isotopically distinct gas reservoirs occurred rapidly during the CAI formation.

Keywords: Calcium-aluminum-rich inclusions, solar nebula, oxygen isotopes, Al-Mg isotope systematic, transmission electron microscopy

1. Introduction

Refractory Ca-Al-rich inclusions (CAIs) are among the oldest solids (4.567 Ga; Connelly et al., 2012) that record the early stages of Solar System formation. CAIs are composed of high-temperature refractory minerals that, based on thermodynamic calculations (Grossman, 1972), are predicted to condense from a cooling gas of solar composition, and so they are commonly thought to reflect primordial materials. Diverse types of CAIs have been identified and extensively studied from different chondrite groups; now we understand that many CAIs are coarse-grained inclusions that formed by various degrees of melting and evaporation of an initial dust population comprised of earlier, more primitive condensates. In particular, the CV chondrite group contains relatively

large and abundant igneous CAIs (MacPherson, 2014). Studies of mineralogical and isotopic record(s) of these igneous CAIs can therefore be used to constrain the range of high-temperature conditions, and possible changing nebular reservoirs, that primordial materials experienced.

Significant variations in oxygen isotopic compositions have been revealed by in situ measurements within and among igneous CAIs in CV chondrites, and the origin of these variations has been a subject of considerable debate. Many minerals in the inclusion, including melilite, anorthite, and Al,Ti-diopside, appear to have various degrees of ^{16}O depletion, compared to hibonite and spinel that are consistently ^{16}O-rich. Such oxygen isotopic heterogeneity in igneous CAIs may have been established in the solar nebula by (1) gas-melt exchange during one or more melting events and subsequent mineral crystallization (e.g., Yurimoto et al., 1998; Fagan et al., 2004; Yoshitake et al., 2005; Aléon et al., 2007; Aléon, 2016; Kawasaki et al., 2018; Simon et al., 2019; Suzumura et al., 2021) or (2) gas-solid exchange during one or more nebular heating events after CAI solidification (Simon et al., 2011, 2016). Importantly, CV chondrites, even those from the reduced subgroup, are known to have preserved a record of fluid-assisted metasomatism and thermal metamorphism at a peak temperature of ~300–500°C on their parent body (Brearley and Krot, 2013). These alteration processes likely modified the primary nebular signatures of oxygen isotopes in igneous CAIs via (3) mineralogically controlled exchange with an ^{16}O-poor fluid on the CV chondrite parent body (e.g., Krot et al., 2019, 2021, 2022). Therefore, the observed heterogeneous distributions in oxygen isotopes among and within individual minerals from different igneous CAIs in CV chondrites could have been the result of combined and complex effects of oxygen isotopic exchanges with gas reservoirs in the solar nebula, with aqueous fluids on the parent body, or both.

Considerable variations in initial ^{26}Al/^{27}Al ratios, denoted by $(^{26}\mathrm{Al}/^{27}\mathrm{Al})_0$, have been indicated by high-precision mineral isochron studies of igneous CAIs from CV chondrites. To first order, the ^{26}Al-^{26}Mg isotope systematics ($t_{1/2}$ = 0.705 Ma; Norris et al., 1983) provide high-resolution timing constraints for the first ~4 Ma of Solar System history. Previous secondary ion mass spectrometry (SIMS) studies of compact Type A (CTA), Type B, and forsterite-bearing Type B (FoB) CAIs reported a spread in $(^{26}\mathrm{Al}/^{27}\mathrm{Al})_0$ from 5.2×10^{-5} to 4.2×10^{-5} (Kita et al., 2012; MacPherson et al., 2012, 2017, 2018; Kawasaki et al., 2018, 2021; Han et al., 2020). This spread suggests that igneous CAIs began to form as early as the canonical ^{26}Al/^{27}Al value (5.23×10^{-5}; Jacobsen et al., 2008) was established, and some of them were later reprocessed by repeated high-

temperature events that occurred for at least ~0.4 Ma in the solar nebula resulting in partial to complete melting and/or evaporation. Evidence for nebular resetting of $^{26}Al/^{27}Al$ in CAIs was also provided by multicollector inductively coupled plasma mass spectrometry measurements of CTA and Type B CAIs from CV chondrites (Young et al., 2005; Simon et al., 2005; Simon and Young, 2011). Thus, igneous CAIs from CV chondrites appear to have preserved a record of interaction and exchange with spatially and/or temporally distinct gas reservoir(s) in the protoplanetary disk.

Here we present the results of coordinated analyses of petrology, mineralogy, microstructures, and oxygen and Al-Mg isotopic compositions of a Type B CAI, ''*Big Guy*", from the reduced CV3 chondrite Vigarano. Coordinated analyses using multiple ion- and electron-beam techniques are crucial to fully decipher complex processes that the CAI experienced in the nebular and asteroidal settings. Our goals were: (1) to better characterize mineralogical and chemical variations across the CAI, (2) to search for any variations in oxygen and Mg isotopic compositions across the CAI, (3) to determine the timing of CAI formation relative to the assumed "time zero" represented by $^{26}Al/^{27}Al = 5.23\times10^{-5}$ (Jacobsen et al., 2008) using the ^{26}Al-^{26}Mg chronology, (4) to evaluate mineralogical and isotopic evidence for secondary parent body alteration that the CAI may have experienced, and finally (5) constrain the formation conditions of the CAI in the solar nebula. Han et al. (2020) is a companion study that focused on the Wark-Lovering (WL) rim on the same inclusion to investigate the origin and nature of WL rims.

2. Methods

2.1. Electron microscopy

The CAI *Big Guy* (Fig. 1) in a thin section of Vigarano (USMNH 447) was initially characterized using a JEOL 7600F scanning electron microscope (SEM), as well as CAMECA SX-100 and JEOL JXA-8530F electron probe microanalyzers (EPMAs) at NASA Johnson Space Center (JSC). The EPMA measurements were performed at 15 kV accelerating voltage, 30 nA beam current, and 1 μm spot size. After the oxygen and Al-Mg isotope analyses by SIMS, a JEOL JXA-8530F EPMA at Korea Polar Research Institute (KOPRI) was utilized to obtain chemical compositions of melilite and pyroxene by measuring ≥4 points as close as possible (within 5–7 μm) to their SIMS spots. Average values of åkermanite ($Åk^{av}$) content in melilite and TiO_2 (TiO_2^{av}) content in pyroxene were used to find any correlations with their oxygen isotopic composition, as discussed in Section 3.2. These EPMA measurements were performed at 15 kV accelerating

voltage, 20 nA beam current, and 1 μm spot size.

Three electron-transparent sections were prepared from the core and the core-mantle boundary of the CAI, using a FEI Quanta 3D 600 dual beam focused ion beam (FIB)/SEM at NASA JSC. In addition, three additional sections were cut from the mantle-rim boundary, and their transmission electron microscopy (TEM) observations were presented in Han et al. (2020). The FIB sections were examined using a 200kV JEOL 2500SE field-emission scanning TEM (STEM) at NASA JSC. Bright-field (BF) and dark-field (DF) STEM images, high-resolution (HR) TEM images, and selected area electron diffraction patterns were acquired and processed using GATAN Digital Microscopy Suite® imaging software. In addition, quantitative chemical microanalyses and elemental mapping were carried out using a Thermo-Noran thin-window energy dispersive X-ray spectrometer. Elemental X-ray maps were obtained using STEM raster mode with a scanned probe size of 2 nm and a dwell time of 50 μs/pixel. Data reduction was performed using the Cliff-Lorimer thin film approximation with experimental and theoretical K-factors.

2.2. SIMS measurements

Han et al. (2020) presented oxygen and Al-Mg isotopic compositions of the CAI *Big Guy*, with a focus on its WL rim, obtained using the CAMECA NanoSIMS 50L ion microprobe at NASA JSC and the CAMECA ims-1290 ion microprobe at UCLA, respectively. For this study, new oxygen and Al-Mg isotope measurements from the same inclusion were made with the UCLA ims-1290 ion microprobe.

Given the relatively large errors associated with the NanoSIMS oxygen isotope data reported in Han et al. (2020), we re-analyzed oxygen isotopic compositions of melilite, spinel, and diopside in *Big Guy* in two sessions using the ims-1290 ion microprobe. In session one (3O-I), a ~4 nA Cs^+ beam focused into a ~10 μm spot was used to analyze coarse melilite grains in the CAI interior, and three oxygen isotopes were collected simultaneously by using three Faraday cups (FCs). In session two (3O-II), due to the smaller sizes of spinel and diopside in the CAI interior and the WL rim, a ~50 pA Cs^+ beam focused into a ~2–3 μm spot was used, and secondary ions of $^{16}O^-$, $^{17}O^-$, and $^{18}O^-$ were detected simultaneously on a multicollector FC, the axial electron multiplier (EM), and a multicollector EM, respectively. A normal incidence electron gun was used for charge compensation. Ion intensities were corrected for backgrounds and yields (FC) or

deadtime (EM) as appropriate for each detector. The mass resolution power (MRP, defined as M/ΔM) was set at ~5500 on mass 17 to ensure that the contribution of $^{16}OH^-$ to $^{17}O^-$ was negligible. Oxygen isotopic compositions are reported in delta notation relative to Standard Mean Ocean Water (SMOW), with $\delta^{17,18}O$ (‰) = $[((^{17,18}O/^{16}O)_{sample}/(^{17,18}O/^{16}O)_{SMOW})\times1]\times1000$. Vertical deviations from the terrestrial fractionation line were calculated as $\Delta^{17}O$ (‰) = $\delta^{17}O-0.52\times\delta^{18}O$. Instrumental fractionation was corrected using Madagascar hibonite for melilite in session one (3O-I) and Burma spinel for spinel, Synthetic gehlenite (Yurimoto et al., 1994) for melilite, and San Carlos pyroxene for diopside in session two (3O-II). Reported errors on $\delta^{18}O$, $\delta^{17}O$, and $\Delta^{17}O$ are 2σ standard deviations obtained from repeated measurements of standards, which are ~0.8‰, ~0.5‰, and ~0.5‰, respectively, for session one (3O-I) and ~0.8‰, ~1.0‰, and ~0.9‰ for session two (3O-II). Overall, our new ims-1290 ion microprobe data are consistent within errors with the NanoSIMS data (Han et al., 2020) but of higher precision; thus, only the new data acquired here are discussed in detail below. One should note that only $\Delta^{17}O$ values are discussed below, as $\delta^{17,18}O$ in melilite and diopside could be a few ‰ deviated from the true values due to the lack of matrix-matching standards to correct for the matrix effects, which are purely mass dependent.

Han et al. (2020) applied peak-jumping monocollection to analyze melilite from the CAI interior, which resulted in somewhat a larger uncertainty on $\Delta^{26}Mg^*$ values. Such uncertainty precluded a precise determination of $(^{26}Al/^{27}Al)_0$ from its isochron diagram, although the melilite data were broadly consistent with high-precision multicollection data obtained from hibonite, spinel, and diopside in the CAI interior and the WL rim. Thus, we re-measured Al-Mg isotopic compositions of melilite, spinel, and Al,Ti-diopside from the CAI interior using high-precision multicollection with FCs, as described in Han et al. (2020).

3. Results

3.1. Mineralogy and petrology

The Vigarano CAI *Big Guy* is a 1,200×750 μm fragment of a coarse-grained Type B inclusion with a classic core-mantle-rim structure (Fig. 1). The core, ~650 μm across, consists of a polycrystalline mass of blocky Al,Ti-diopside grains and poikilitic euhedral spinel crystals (Fig. 2). The core diopside appears to be zoned outwards from Ti-rich, Mg-poor to Ti-poor, Mg-rich (Fig. 2b), with a range of 6.7–16.5 wt% TiO_2 and 16.7–21.3 wt% Al_2O_3 (Fig. 3a). The core edges are highly convoluted and exhibit Ti enrichments (Figs. 2f-g). TEM analyses show that Al,Ti-

diopside (15 wt% TiO_2) in the core edge is rimmed by a thin (~200–500 nm) layer of Al-diopside (<3 wt% TiO_2), and these two diopsides are chemically distinct but crystallographically continuous (Fig. 4). Although both diopsides have relatively constant Al_2O_3 contents (15–17 wt%), the core Al,Ti-diopside shows Ti enrichments and corresponding Si depletions within ~20 nm of the grain boundary (Fig. 4b), contributing to the Ti enrichments along the core edge. Locally, symplectic intergrowths of perovskite, melilite, and Al,Ti-diopside occur at the core-mantle boundary (Figs. 2d-e). TEM analyses show that the perovskite grains in these intergrowths are typically elongated and partially surrounded by Al,Ti-diopside, embedded in melilite (Fig. 5a).

The mantle is composed predominantly of coarse melilite grains, ~250–450 μm in size. These melilite grains radiate from the WL rim towards the core and are strongly zoned along their lengths, indicating inward growth during crystallization of a CAI melt (MacPherson and Grossman, 1981). In general, the åkermanite content varies systematically (Fig. 3b), gradually decreasing from 55 mol% to 15 mol% over a distance of ~50–200 μm from the core and then becoming relatively constant (~10–15 mol%) throughout the rest of the mantle. Notably, the åkermanite content decreases down to 0 mol% within ~20 μm from the WL rim. Based on TEM observations reported in Han et al. (2020), the mantle margin just inside of the WL rim consists of micrometer-sized, pure gehlenite grains with a rare inclusion of grossite.

Spinel occurs as subhedral to euhedral grains poikilitically enclosed in the core and the mantle. Although its grain size and abundance tend to increase inwards, spinel both in the core and the mantle has a uniform composition of nearly pure $MgAl_2O_4$ with 0.3–0.6 wt% V_2O_3 and <0.1wt% FeO. Additionally, perovskite occurs as small grains attached to spinel crystals in the core and the mantle (Figs. 2d-g), but rarely as interstitial grains between melilite grains in the mantle.

Finally, the CAI is surrounded by a classic multi-layered WL rim sequence (from the inside outwards): hibonite, spinel with hibonite and perovskite, melilite partially replaced by anorthite, zoned diopside grading outwards from Al,Ti-rich to Al,Ti-poor, and forsteritic olivine. A detailed microstructural and isotopic study of the WL rim was presented in Han et al. (2020). An accretionary rim is also present on the WL rim and is dominated by forsteritic olivine with minor metal and micro-CAIs (Fig. 1).

Despite being found in a reduced CV3 chondrite, *Big Guy* does show minor effects of secondary parent body alteration, similar to other coarse-grained CAIs in the same meteorite (Brearley and Krot, 2013). The principal manifestation of such processes is the widespread, yet

heterogeneous, Fe enrichments along cracks and grain boundaries throughout the inclusion (Fig. 2c). TEM analyses of the core-mantle boundary reveal that ubiquitous Fe-rich veins up to ~1.5 μm in thickness occur along the grain boundaries of Al,Ti-diopside and melilite and commonly cross-cut through melilite grains (Figs. 4a, 5). These veins are typically porous and poorly crystalline, and their interfaces with melilite appear highly irregular and commonly embayed into melilite grains. Some veins between melilite grains are zoned (Fig. 5b); the grains are walled by a porous, fibrous layer rich in phyllosilicates, whereas the middle of the veins is relatively denser and more Fe-rich. Phyllosilicates show a basal spacing of ~0.7 nm corresponding to serpentine (Fig. 5c). The Fe-rich layer is inferred as ferrihydrite and possibly nanophase magnetite, based on the observed basal spacings of 0.20 nm, 0.25 nm, and 0.52 nm (Lee et al., 1996). At the mantle-rim boundary, amorphous Fe-rich veins (≤0.5 μm in thickness) are developed along grain boundaries of melilite and hibonite and into melilite grains.

3.2. Oxygen isotopic compositions

The oxygen isotopic compositions of the CAI *Big Guy* are plotted in Figure 6 and listed in Table 1. Spinel is uniformly ^{16}O-rich with $\Delta^{17}O \leq -23‰$, regardless of its location. The WL rim diopside is also ^{16}O-rich with $\Delta^{17}O = -23‰$. In contrast, Al,Ti-diopside in the core and melilite in the mantle are relatively ^{16}O-depleted to various degrees, with $\Delta^{17}O$ values ranging from −11‰ to −18‰ and from −3‰ to −15‰, respectively.

The observed variations in oxygen isotopic compositions of pyroxene and melilite in *Big Guy* appear to be correlated with their chemical compositions. Figure 6a shows a positive correlation between $\Delta^{17}O$ values and TiO_2 contents of Al,Ti-diopside in the core and diopside in the WL rim. Such a relationship has been reported for Al,Ti-diopside in CTA and Type B CAIs (Aléon, 2016; Kawasaki et al., 2018; Suzumura et al., 2021; Krot et al., 2022; MacPherson et al., 2022). Although different CAIs display different ranges of oxygen isotopic and chemical compositions of Al,Ti-diopside, their $\Delta^{17}O$ variations flatten out towards −23‰ with decreasing TiO_2 content in the diopside. Figure 6b shows a relationship between $\Delta^{17}O$ values and the åkermanite contents of melilite in the mantle. The $\Delta^{17}O$ values ≤−10‰ can be observed only in melilite with $Åk_{<15}$. Melilite with $Åk_{>15}$ is more ^{16}O-poor, with $\Delta^{17}O$ ranging from −3‰ to −9‰. A similar trend between oxygen isotopic compositions and chemical zoning of melilite ($Åk_{<30}$) was observed for the CTA CAI *E49* in Efremovka (Aléon et al., 2007). In contrast, relatively

constant ^{16}O-poor compositions were observed from melilite with Åk up to ~60 mol% in CTA and Type B1 CAIs (Kawasaki et al., 2018; Suzumura et al., 2021). Figures 6c and 6d show the spatial distribution of oxygen isotopic compositions on the maps of TiO_2 content of the core Al,Ti-diopside and åkermanite content of the mantle melilite, suggesting no simple monotonic change of Δ^{17}O variations in these two phases as a function of distance from the matrix. In particular, the most ^{16}O-enriched melilite with $\Delta^{17}O \approx -15$‰ is observed in the center of the mantle where its åkermanite content is lowest (~15 mol%), and a gradual decrease in ^{16}O enrichment occurs towards both the core ($\Delta^{17}O \approx -3$‰) and the mantle margin ($\Delta^{17}O \approx -7$‰). The Δ^{17}O increase towards the core is accompanied with a gradual Mg enrichment in melilite up to Åk ≈ 55 mol%, whereas, in the mantle margin, the Δ^{17}O values do not correlate with the chemical compositions of melilite.

3.3. Al-Mg isotopic compositions

The Al-Mg isotope data of spinel, Al,Ti-diopside, and melilite in the CAI *Big Guy* are plotted in Figure 7 and listed in Table 2. These high-precision multicollection data define a single isochron, albeit with some scatter (reduced $\chi^2 = 4.6$) in the melilite data. The slope and the intercept of the isochron correspond to $(^{26}Al/^{27}Al)_0 = (4.93\pm0.18)\times10^{-5}$ and $\Delta^{26}Mg_0^* = -0.01\pm0.1$‰ (2σ), respectively. This inferred $(^{26}Al/^{27}Al)_0$ ratio is consistent with that reported in Han et al. (2020) derived from the data obtained with the same instrument of spinel and Al,Ti-diopside from the CAI interior, and hibonite, spinel, and diopside from the WL rim.

All minerals in the CAI interior exhibit high δ^{25}Mg values. Spinel and Al,Ti-diopside have relatively constant δ^{25}Mg values of ~11‰ and ~9‰, respectively. The δ^{25}Mg values of melilite show a range from 6.5‰ to 8.4‰. In contrast, Han et al. (2020) reported a distinctly lower range of δ^{25}Mg values (mostly <0‰) in the WL rim minerals.

4. Discussion

4.1. Mineralogical constraints

The Vigarano CAI *Big Guy* has diagnostic mineralogical and petrologic features of Type B CAIs so that it can be interpreted as an igneous object that was once molten (e.g., MacPherson and Grossman, 1981). The bulk composition of *Big Guy*, estimated by using the method described in Simon and Grossman (2004), is 25 SiO_2, 3 TiO_2, 33 Al_2O_3, 8 MgO, and 31 CaO, (in wt%). This composition is marginally within a previously reported range for Type B CAIs, and the observed

compositional ranges of melilite and Al,Ti-diopside in the CAI interior are more comparable to those reported from Type B1 than Type B2 CAIs (Wark and Lovering, 1982; Simon and Grossman, 2004, 2006). The bulk composition of *Big Guy* plots above the saturation surface of melilite on the gehlenite-anorthite-forsterite phase diagram projected from spinel, suggesting that spinel crystallizes first, followed by melilite and finally Al,Ti-diopside (Stolper, 1982). This is consistent with our petrographic observations, from which a crystallization sequence of spinel, followed by melilite and finally Al,Ti-diopside (Ti-rich to Ti-poor), can be inferred. Finally, an igneous origin of *Big Guy* is supported by mass-dependent fractionation of Mg isotopes determined from spinel, Al,Ti-diopside, and melilite in the CAI interior (δ^{25}Mg = ~7–11‰; Table 2), which is consistent with that associated with evaporation of Type B CAI-like melts in vacuum (Richter et al., 2007).

Our TEM observations of the core-mantle boundary from *Big Guy* provide evidence for a late-stage crystallization history of the CAI core. Along the highly irregular core-mantle boundary, Al,Ti-diopside is rimmed by Al-diopside (Fig. 4), and the local symplectic intergrowths of perovskite grains and partially surrounding Al,Ti-diopside are embedded in melilite (Fig. 5a). We infer that a residual melt was trapped between Al,Ti-diopside and melilite after the formation of the CAI core. The core Al,Ti-diopside, which most Ti in the original melt was incorporated into, would have provided a substrate for additional crystallization of crystallographically oriented Al-diopside, forming the chemically evolved thin rim layer. When the Al-diopside rim layer was crystallizing, some local melts may have evolved towards Ti-enriched composition and thus resulted in crystallization of symplectic intergrowths of fine-grained perovskite and Al,Ti-diopide (Simon et al., 1999). Alternatively, the characteristics along the core-mantle boundary may be a result of multiple short-lived heating events that led to various degrees of partial melting during the CAI formation history. If short-lived heating occurred around the solidus temperature of the CAI melt (~1250°C; Stolper, 1982) after the CAI solidification, minor Al,Ti-diopside and åkermanitic melilite may have melted as a thin veneer on the surface of the core (e.g., Aléon et al., 2007; Kawasaki et al., 2018), resulting in rapid crystallization of the Al-diopside rim layer and the symplectic intergrowths of perovskite and Al,Ti-diopside.

After the crystallization of the Al-diopside rim layer onto the core Al,Ti-diopside, an interdiffusion involving the coupled substitution of $Ti^{4+} + 2Al^{3+} \leftrightarrow Mg^{2+} + 2Si^{4+}$ likely occurred between these two diopsides, resulting in very narrow Ti-enrichment within ~20 nm of the Al,Ti-diopside grain edge (Fig. 4b). The interdiffusion rate may be very slow because the substitution

involves six cations, as noted by Simon and Grossman (2006). To induce the interdiffusion between Al,Ti-diopside and Al-diopside after the CAI solidification, late high-temperature nebular processing, such as a flash heating event responsible for the WL rim formation (Wark and Boynton, 2001; Han et al., 2020), is therefore more effective than thermal diffusion in response to parent body metamorphism.

4.1.1. Evidence for parent body alteration

Our TEM observations provide evidence for a low degree of secondary parent body alteration processing of the CAI *Big Guy*. These observations are preferentially apparent with melilite and include the presence of poorly crystalline Fe-rich veins and their ragged interfaces with adjacent melilite (Figs. 4a, 5). Similarly, Paque et al. (2009) observed amorphous OH-bearing veins that share corroded interfaces with melilite in a Type B1 CAI *3537-2* from the reduced CV chondrite Leoville that was classified as the same petrologic subtype as Vigarano (Bonal et al., 2006). In addition, previous hydrothermal experiments conducted at 200–400°C for up to 7 days demonstrated that melilite was dissolved readily by fluids to release Al, Si, and Ca, forming hydrous phases such as Na zeolite (Nomura and Miyamoto 1998; Ichimura et al. 2017). We therefore conclude that the Fe-rich veins formed by partial dissolution of primary melilite in response to incipient aqueous alteration in a low-temperature, oxidizing parent body environment. In particular, the observed zonation in the veins between melilite grains (Fig. 5b) indicates that primary melilite has been partially replaced by phyllosilicates during aqueous alteration, while Fe-rich oxides precipitated from aqueous fluids into an open space formed by the dissolution of primary melilite. However, melilite in immediate contact with the veins contains no detectable Na and Fe, suggesting that parent body processing seems to only have minimal effects on primary characteristics of the CAI inherited during its formation in the solar nebula.

Our interpretation is consistent with TEM studies of the matrix mineralogy in Vigarano. Lee et al. (1996) observed minor amounts of ferrihydrite and smectite as fine intergrowths between Mg-Fe silicate (mostly partially equilibrated FeO-rich olivine) and oxide grains in the Vigarano matrix. These observations were interpreted as a result of low-temperature (<150°C) aqueous alteration, followed by metamorphic heating (~400–500°C) in the parent body environment. In addition, Abreu and Brearley (2011) reported the abundance of FeO-rich olivine with heterogeneous compositions, grain sizes, and morphologies in the Vigarano matrix. These

observations were interpreted to indicate that FeO-rich olivine formed by recrystallization of amorphous silicate precursor in the presence of limited amounts of fluids during the early stages of metamorphic heating on the parent body. However, the widespread occurrence of amorphous carbon observed in the Vigarano matrix likely reflects the primary nebular signature of organic material, demonstrating a very limited, mild degree of thermal processing in the asteroidal setting (Brearley, 1990; Abreu and Brearley, 2011).

4.2. Oxygen isotopic constraints

The CAI *Big Guy* exhibits considerable heterogeneity in oxygen isotopic composition, with $\Delta^{17}O$ ranging from solar-like −25‰ to planetary-like −3‰ (Table 1). Spinel is uniformly ^{16}O-rich, but Al,Ti-diopside and melilite are ^{16}O-depleted to various degrees, which appear to correlate with their chemistry (Fig. 6). *Big Guy* is unique in that the mantle melilite is characterized by variable $\Delta^{17}O$ (Fig. 6d), with the center of the mantle being the most ^{16}O-enriched ($\Delta^{17}O \approx -15$‰) and the edges (in contact with the core and the WL rim) being relatively depleted ($\Delta^{17}O \approx -3$‰ and −7‰). The coupled chemical and oxygen isotopic variations suggest the CAI underwent complicated thermal and crystal growth histories. Below we explore possible mechanisms for the origin of heterogeneous oxygen isotopic compositions observed in *Big Guy*, taken together with a quantitative consideration of oxygen diffusion rates in CAI minerals. We note that most of these rates were experimentally determined in dry conditions, which may have been distinctly different from the asteroidal environment in which aqueous fluids were locally interacting with CAI minerals.

4.2.1. Minimal exchange with an ^{16}O-poor fluid

All CV chondrites including Vigarano are known to have experienced mineralogically controlled exchange with an ^{16}O-poor fluid during metamorphic heating on their parent asteroid (Brearley and Krot, 2013). Aqueous fluids with $\Delta^{17}O = -3\pm2$‰ were inferred from oxygen isotopic compositions of secondary minerals produced during metasomatic alteration of Allende coarse-grained CAIs (Krot et al., 2021, 2022). Similar ^{16}O-poor compositions are observed from some melilite analyses in *Big Guy* (Table 1). As discussed in Section 4.1.1, melilite has been preferentially dissolved and replaced by Fe-rich veins (Figs. 4a, 5), suggesting that this primary phase is susceptible to interactions with aqueous fluids on the parent body. However, the

correlation between oxygen isotopic compositions and chemistry observed from Al,Ti-diopside and melilite (Fig. 6) would have not been expected through interactions with an ^{16}O-poor fluid in the asteroidal setting. Therefore, the parent body alteration scenario seems unlikely for the origin of the observed disequilibrium in oxygen isotopes among coexisting minerals in *Big Guy*.

This interpretation is supported by our oxygen isotope data measured from the WL rim of *Big Guy*. The SIMS analyses show that spinel and diopside in the WL rim are ^{16}O-rich with Δ^{17}O ≤ -23‰ (Table 1), which agrees well with the NanoSIMS data of all the WL rim minerals reported in Han et al. (2020). The Δ^{17}O values of the WL rim melilite and anorthite, -20.0 ± 3.1‰ and -21.8 ± 3.1‰, respectively, are only marginally higher than coexisting spinel and diopside. The oxygen diffusivity in anorthite is about 10 times faster than that in melilite, and ~10 orders of magnitude faster than those of spinel and diopside at 300–400°C (Fig. 8a; Yurimoto et al., 1989; Ryerson and McKeegan, 1994). Under wet conditions, oxygen diffusion in anorthite is enhanced by 5–6 orders of magnitude compared to that under dry conditions (Fig. 8a; Giletti et al., 1978; Elphick et al., 1988). Therefore, anorthite would be the most susceptible to oxygen isotopic exchange with an ^{16}O-poor fluid in response to thermal metamorphism on the parent body. Since anorthite grains in the WL rim, which are typically 5 μm in size (Han et al. 2020), still retain the original oxygen isotopic compositions, the maximum heating duration at peak metamorphic temperatures of 300–400°C (Busemann et al., 2007) cannot be longer than ~50 years (Fig. 9). Diffusive exchange for this relatively short timescale would not have affected oxygen isotopic compositions over lengths of <1 μm for other mineral phases, even if the oxygen diffusion process was enhanced by aqueous fluids during thermal metamorphism. Thus, the observed ^{16}O depletions over a distance of 50–100 μm in the edges of the mantle melilite cannot be accounted for by metamorphic heating on a timescale of ~50 years.

Additional evidence against the parent body origin of oxygen isotopic variations in the mantle melilite comes from the spinel chemistry. It is known that Mg-Fe interdiffusion in spinel is 2–3 orders of magnitude faster than oxygen self-diffusion in melilite at 300–400°C (Fig. 8a; Freer and O'Reilly, 1980; Yurimoto et al., 1989). If oxygen isotopic compositions of the mantle melilite were largely modified during thermal metamorphism on the parent body, FeO in spinel, particularly in the WL rim, should have been greatly increased through Fe diffusion from the matrix as well. However, spinel contains only minor FeO up to 1.1 wt%, regardless of its location and size. We thus conclude that the observed oxygen isotopic variations across *Big Guy* were

established in the solar nebula, and there was minimal oxygen isotopic exchange with an ^{16}O-poor fluid on the Vigarano parent body.

4.2.2. Nebular exchange recorded in the core and the mantle

As indicated by its igneous texture, the CAI *Big Guy* crystallized from a melt, with spinel being the first phase to form, followed by melilite and Al,Ti-diopside. The uniform, solar-like ^{16}O-rich compositions ($\Delta^{17}O \approx -23‰$) of euhedral spinel crystals in the CAI interior (Table 1) and the slow oxygen diffusivity in spinel (Fig. 9; Ryerson and McKeegan, 1994) suggest that the original melt (and likely the precursor material to this melt) was characterized by $\Delta^{17}O = -23‰$. Equally, fine-grained WL rim minerals are ^{16}O-rich, which contrasts sharply with variably ^{16}O-depleted Al,Ti-diopside and melilite in the CAI interior (Fig. 6, Table 1; Han et al., 2020). Therefore, the heterogenous oxygen isotopic compositions of Al,Ti-diopside and melilite in the CAI interior must have been established between the formation of spinel in the CAI interior and the WL rim, the latter of which represents the final stage of the entire CAI formation involving condensation in an ^{16}O-rich gas (Han et al., 2020). Two mechanisms in the nebular setting are considered below.

In the first scenario, Al,Ti-diopside and melilite in the CAI interior may have recorded an evolving oxygen isotopic composition of a crystallizing melt that was exposed to gas reservoirs of different oxygen isotopic compositions (e.g., Yurimoto et al., 1998; Yoshitake et al., 2005; Aléon et al., 2007; Aléon, 2016; Kawasaki et al., 2018; Suzumura et al., 2021). The strong zonation of åkermanite contents in the mantle melilite (Fig. 3b) and the Al and Ti zonation in the core Al,Ti-diopside (Fig. 2b), combined with their texture, indicate inward growth of these two phases during radiative cooling from a molten droplet (MacPherson and Grossman, 1981; Simon and Grossman, 2006). Therefore, the observed correlations between oxygen isotopic composition and chemistry of Al,Ti-diopside and melilite (Fig. 6) suggest that the oxygen isotopic variations were established during crystallization of these two phases from a cooling melt.

Aléon et al. (2007) argued that oxygen isotopic equilibration of an ^{16}O-rich melt interior with an ^{16}O-poor gas during melilite crystallization can be reached via oxygen diffusion in interstitial melts between crystallizing melilite grains inward from the melt surface, owing to fast kinetics of oxygen diffusion in Ca,Al-rich melt (Oishi et al., 1974; Yamamoto et al., 2021, 2022). Likewise, Kawasaki et al. (2018) proposed a melt channelway mechanism that enabled oxygen isotopic exchange between an ^{16}O-poor melt in the inclusion interior and an ^{16}O-rich gas at the

inclusion surface during Al,Ti-diopside crystallization, after the formation of the mantle melilite. Indeed, Yamamoto et al. (2021, 2022) experimentally demonstrated that oxygen isotopes were exchanged at the melt surface and simultaneously diffused into the melt interior, based on isothermal oxygen isotope exchange experiments on Type B CAI-like melt with low-pressure H_2O and CO gases above the liquidus temperature of melilite at 1420℃ and 1460℃. Alternatively, a nebular gas may have penetrated through grain boundaries and crack networks of early crystallizing melilite crystals into a melt in the inclusion center (Kawasaki et al., 2018). We therefore envisage the following steps by assuming that oxygen isotopes were continuously transported and diffused into the melt interior.

1) The CAI precursor that formed initially in an ^{16}O-rich gas ($\Delta^{17}O \approx -23‰$) was heated to temperatures above the liquidus temperature of spinel (~1550℃; Stolper, 1982; Stolper and Paque, 1986), producing a melt having a homogenous ^{16}O-rich composition. Spinel crystallized first from this melt and was ^{16}O-rich. Alternatively, the spinel may have been a relict phase that was originally ^{16}O-rich and survived after a melting event at temperatures of ~1400–1550℃, the liquidus temperature between spinel and melilite (Stolper, 1982; Stolper and Paque, 1986; Yamamoto et al., 2021).
2) As the ^{16}O-rich melt underwent oxygen isotopic exchange with an ^{16}O-poor gas, melilite crystals with $\Delta^{17}O \approx -15‰$ and Åk ≈ 15 mol% began to nucleate on the surface of this melt at ~1450℃ (Mendybaev et al., 2006; Kamibayashi et al., 2021). Upon cooling, crystallizing melilite continued to grow inward, as it became increasing in Åk content up to ~55 mol% but depleted in ^{16}O down to $\Delta^{17}O \approx -3‰$.
3) After melilite largely formed, this partial melt was then exposed to an ^{16}O-rich gas and diffusively equilibrated with this gas during crystallization of Al,Ti-diopside at temperatures of ~1100–1230℃ (Stolper, 1982; Stolper and Paque, 1986). The first crystallizing diopside was the most depleted in ^{16}O ($\Delta^{17}O \approx -11‰$) but the most enriched in TiO_2 up to ~17 wt%. As cooling proceeded, diopside became progressively enriched in ^{16}O up to $\Delta^{17}O \approx -18‰$ while simultaneously decreasing in TiO_2 down to ~7 wt%.

This proposed gas-melt exchange scenario may be realized both in the context of a single melting event and multiple melting events, as suggested by Kawasaki et al. (2018) who also observed a similar correlation between oxygen isotopic compositions and TiO_2 contents (i.e.,

crystal growth direction) of Al,Ti-diopside grains in the Allende CAI *TS34*. During a single melting event, continuous exchange would have occurred with the surrounding nebular gas whose composition changed from ^{16}O-poor to ^{16}O-rich. The melilite crystallization must have stopped as soon as the melt began to exchange oxygen isotopes with an ^{16}O-rich nebular gas. Therefore, the first crystallizing (i.e., the most Ti-rich) Al,Ti-diopside became the most ^{16}O-depleted within the core, but slightly more ^{16}O-enriched than the last crystallizing (i.e., the most Mg-rich) melilite (Figs. 6c-d). Alternatively, multiple heating events may have taken place in nebular gas reservoirs of different oxygen isotopic compositions. After the CAI interior first crystallized from a melt in an ^{16}O-poor nebular gas, a later heating event would have occurred in an ^{16}O-rich nebular gas around the solidus temperature of the CAI melt (~1250°C; Stolper, 1982). Subsequent partial melting resulted in progressive exchange with the ^{16}O-rich nebular gas during re-crystallization of Al,Ti-diopside, so this phase became gradually ^{16}O-enriched. The full equilibration of oxygen isotopic compositions between melilite and Al,Ti-diopside would not be expected, as indicated by a difference in oxygen isotopic compositions at the interface between these two phases (Figs. 6c-d).

In the second scenario, after initial crystallization of the CAI interior from an ^{16}O-rich melt, melilite and Al,Ti-diopside may have experienced solid-state diffusive exchange with an ^{16}O-poor gas reservoir in the solar nebula (Simon et al., 2011, 2016). This later exchange should have occurred before WL rim formation; otherwise, fine-grained anorthite and melilite in the WL rim would have been ^{16}O-poor. Yet, this scenario seems problematic. Solid-state diffusion would be expected to produce a Δ^{17}O profile having the most ^{16}O depletion at crystal edges and gradual ^{16}O enrichment moving inwards. This is not the case for *Big Guy* in which ^{16}O depletions are correlated with Mg enrichments in the mantle melilite and Ti enrichments in the core Al,Ti-diopside (Fig. 6). To be consistent with the gas-solid exchange scenario, it must experimentally demonstrate that there is a correlation between oxygen diffusion rates and Ti contents in diopside, with Al,Ti-diopside being the most susceptible to oxygen diffusive exchange (MacPherson et al., 2022), and also that oxygen diffusion in Al,Ti-diopside should be similar to or even faster than that in gehlenite. Nonetheless, because oxygen diffusion in melilite is 2–3 orders of magnitude faster than that in diopside below the solidus temperature of melilite, at 1100–1400°C (Fig. 8b), any diffusive exchange processes that may have disturbed oxygen isotopic compositions in the entire mantle melilite should still result in no or minimal modification on the original oxygen isotopic

compositions of diopside, even in the outermost core (Fig. 10). In other words, if the observed oxygen isotopic variation in the core Al,Ti-diopside originated from solid-state diffusion, the mantle melilite could not have retained any signature of internally heterogenous oxygen isotopic compositions. A partial equilibration of Mg contents in the mantle melilite would also be expected as Mg diffusion in melilite becomes faster than its oxygen diffusion with increasing temperature (Fig. 8b). Therefore, any subsequent partial melting event would be necessary at temperatures higher than the liquidus temperature of melilite to reset a relationship between chemical and oxygen isotopic compositions established via solid-state diffusion in the mantle melilite. However, such an event would likely lead to a partial to complete melting of the core Al,Ti-diopside surrounded by the mantle melilite. Overall, because of the observed compositional trends in Al,Ti-diopside and melilite, gas-solid exchange event(s) are unlikely to explain the observed heterogenous distribution of oxygen isotopes in the CAI core and mantle.

In all scenarios discussed above, the oxygen isotopic heterogeneity observed in *Big Guy* involves at least two isotopically distinct (^{16}O-rich and ^{16}O-poor) gas reservoirs in which this CAI formed and evolved prior to WL rim formation (e.g., Yurimoto et al., 1998; Yoshitake et al., 2005; Katayama et al., 2012; Park et al., 2012; Aléon, 2016; Simon et al., 2011, 2016, 2019; Kawasaki et al., 2018; Suzumura et al., 2021). This explanation can be realized in the context of transport of CAIs between gas reservoirs of different isotopic compositions (e.g., Ciesla, 2010; Boss et al., 2012) and/or by fluctuations of oxygen isotopic compositions in CAI-forming regions (e.g., Park et al., 2012; MacPherson et al., 2022).

4.2.3. Enigmatic history of the mantle margin

Han et al. (2020) revealed that the mantle margin of *Big Guy* is mineralogically and texturally different, compared to the underlying mantle composed of coarse, zoned melilite ($Åk_{\sim10–55}$) grains, suggesting its distinct formation event after the mantle solidification. For example, the mantle margin exhibits a gradual decrease in åkermanite content of melilite towards the WL rim, down to $Åk_0$ (Fig. 3b). This zone contains fine-grained gehlenite grains with rare grossite just inside of the WL rim that share a common crystallographic orientation (Han et al., 2020). Likewise, the margins of coarse-grained CAIs from CV chondrites are commonly of higher gehlenitic content ($Åk_{0–10}$) than expected for the first-crystallized melilite from a melt of their bulk composition ($Åk_{\sim10–20}$; e.g., Bullock et al., 2013; Simon et al., 1999). It is likely that this gehlenitic melilite

crystallized from a surficial Ca,Al-enriched melt that formed on the CAI margins by a later flash heating and subsequent evaporative loss of Mg (e.g., Beckett and Stolper, 1994; Simon et al., 1999; Bullock et al., 2013; Han et al., 2020). This high-temperature event may be related to an initial step in the WL rim formation (Wark and Boynton, 2001; Han et al., 2020).

However, the measured isotopic compositions of the mantle margin of *Big Guy* appear to pose a problem in elucidating its formation processes and conditions. The slight ^{16}O depletion is observed from gehlenitic melilite ($Åk_{5.5–11.4}$) in the mantle margin, over less than a few tens of μm from the WL rim (Fig. 6d). If the relatively ^{16}O-poor compositions in this mantle margin resulted from isotopic exchange between melilite and an ^{16}O-poor gas before the WL rim formed, the time required would not be longer than 10 years at 1100–1400°C (Fig. 10). Such a heating duration may have also resulted in diffusive exchange in Mg isotopes over a distance of ~10–30 μm (Fig. 10). Although a detailed survey of oxygen and Mg isotopic compositions in the mantle margin of *Big Guy* is lacking in this study, this zone does not appear to exhibit a greater degree of mass-dependent fractionation favoring higher Mg isotopes relative to the mantle interior (Table 2; Han et al., 2020), as would be expected from surface evaporation of a melt. Similarly, the margins of Type B1 and B2 CAIs are composed of very gehlenitic melilite ($Åk_{0–10}$) characterized by isotopically lower Mg isotopes than in the interiors (Young et al., 2005; Simon et al., 2005; Bullock et al., 2013; Kawasaki et al., 2018). These data suggest that a later Mg isotopic exchange with an external and isotopically normal or subchondritic gas reservoir occurred in the CAI margins to erase the effect of mass-dependent fractionation in Mg isotopes produced during evaporation of a surficial melt (Simon et al., 2005; Bullock et al., 2013; Han et al., 2020). Such exchange may have been initiated during or before the formation of the WL rim spinel and diopside layers having normal or subchondritic Mg isotopic compositions (Simon et al., 2005; Han et al., 2020). Meanwhile, Park et al. (2012) revealed that individual melilite grains in the mantle margin of the Allende CTA CAI *ON01* are reversely zoned, having Mg increase towards their core, that are correlated with progressive ^{16}O depletion. They concluded that this correlation is a record of melilite crystal growth by condensation from a nebular gas in which its pressure was decreasing and also its oxygen isotopic composition was evolving from ^{16}O-poor to ^{16}O-rich (Katayama et al., 2012). Therefore, coordinated studies using high spatial resolution instruments of the margins of coarse-grained CAIs in CV chondrites are required to explore any correlations between chemical and oxygen and Mg isotopic compositions of gehlenitic melilite grains in the CAI margins and to better understand the origin of these melilite

549 grains and their relation to the WL rim formation.
550
551 **4.3. Al-Mg isotopic constraints**
552 Despite a limited degree of Mg isotopic disturbance, as suggested by scatter of a couple of
553 data points beyond the analytical uncertainties (reduced χ^2 = 4.6), our new Al-Mg isotope data of
554 spinel, Al,Ti-diopside, and melilite from the CAI *Big Guy* define a single isochron, with a slope
555 corresponding to $(^{26}Al/^{27}Al)_0 = 4.93\times10^{-5}$ (Fig. 7). This ratio indicates that *Big Guy* crystallized
556 from a melt ~5×10^4 years after the peak formation of large CV CAIs at $^{26}Al/^{27}Al = 5.23\times10^{-5}$, as
557 concluded in Han et al. (2020), and is also consistent with *Big Guy* having been processed in a
558 major nebula-wide heating event proposed by Liu et al. (2019).
559 The Al-Mg isotope data of hibonite, spinel, and diopside from the WL rim also define an
560 isochron that has essentially the same slope as do the CAI interior data, suggesting no resolvable
561 age gap between the formation events of the CAI interior and the WL rim (Han et al., 2020). Since
562 oxygen diffuses ~10 times faster than Mg in melilite at 1100–1400°C (Fig. 8b), if Al-Mg
563 systematics in the mantle melilite had been disturbed during the WL rim formation, significant ^{16}O
564 enrichments would have achieved from the WL rim towards the center of the mantle via exchange
565 with an ambient ^{16}O-rich gas in which the WL rim minerals were condensing. Instead, the mantle
566 margin exhibits relative ^{16}O depletions outwards the WL rim (Fig. 6d). Moreover, as discussed in
567 Section 4.2.1, the preservation of ^{16}O-rich compositions across the WL rim melilite and anorthite
568 (Han et al., 2020) implies that Al-Mg isotopic compositions across the core to the WL rim of the
569 CAI were largely undisturbed by fluid-assisted thermal metamorphism on the parent body, as
570 oxygen diffuses at least ~10 times faster than Mg in melilite and anorthite at 300–400°C (Fig. 8a).
571 Therefore, the lack of any difference in $(^{26}Al/^{27}Al)_0$ inferred from the CAI interior and its WL rim
572 indicates that multiple high-temperature events, as well as oxygen isotopic exchange with ^{16}O-rich
573 and ^{16}O-poor gas reservoirs, should have occurred rapidly, within a short time duration that cannot
574 be resolved by the Al-Mg chronology (Aléon et al., 2007; Kawasaki et al., 2018, 2021).
575
576 **5. Conclusions**
577 Our coordinated mineralogical and oxygen and Al-Mg isotopic analyses of the CAI *Big*
578 *Guy* from Vigarano provide constraints on the history of high-temperature events and reservoir
579 evolution in the early solar nebula. This CAI is typical of Type B CAIs, as an igneous object that

was once molten in which spinel crystallized first, followed by melilite and Al,Ti-diopside. Melilite in the mantle has been preferentially altered in the presence of limited fluids on the parent body, but the overall effects of secondary parent body alteration were minimal on primary nebular characteristics of the CAI.

Importantly, heterogeneous oxygen isotopic compositions are observed among and within constituent minerals in the CAI interior, in contrast to ^{16}O-rich WL rim minerals. Spinel is uniformly ^{16}O-rich with $\Delta^{17}O \leq -23‰$, whereas Al,Ti-diopside in the core and melilite in the mantle are relatively ^{16}O-depleted to various degrees. The $\Delta^{17}O$ values ranging from −11‰ to −18‰ of Al,Ti-diopside are positively correlated with its TiO_2 contents, flattening out towards −23‰ recorded in the WL rim diopside. With $\Delta^{17}O$ values ranging from −3‰ to −15‰, melilite in the CAI mantle shows $\Delta^{17}O$ values ≤−10‰ only when $Åk_{<15}$ but becomes more ^{16}O-poor when $Åk_{>15}$. We conclude that the correlated chemical and oxygen isotopic variations were established during crystallization of melilite and Al,Ti-diopside from a partial melt, while spinel retained the original ^{16}O-rich composition of the CAI precursor. Constraints from oxygen diffusion rates in CAI minerals preclude solid-state diffusive exchange with nebular gases and with parent body fluids to account for such correlated variations. Instead, the partial melt should have isotopically evolved from ^{16}O-rich to ^{16}O-poor during melilite crystallization, then back to ^{16}O-rich during Al,Ti-rich diopside crystallization via exchange with ^{16}O-poor and ^{16}O-rich gas reservoirs during single or multiple heating events.

Our Al-Mg isotopic measurements of spinel, Al,Ti-diopside, and melilite from the CAI interior define a single isochron with $(^{26}Al/^{27}Al)_0 = 4.93\times10^{-5}$, consistent with the WL rim data. Thus, we conclude no resolvable age gap between the formation events of the CAI interior and the WL rim, implying that multiple high-temperature events and oxygen isotopic exchange between the CAI melt and isotopically distinct nebular gases occurred rapidly.

CRediT authorship contribution statement

Jangmi Han: Methodology, Investigation, Writing - Original Draft, Writing - Review & Editing, Funding acquisition. **Changkun Park:** Resources, Investigation, Writing - Original Draft, Writing - Review & Editing. **Ming-Chang Liu:** Resources, Investigation, Writing - Review & Editing, Funding acquisition. **Nozomi Matsuda:** Investigation, Writing - Review & Editing. **Justin I. Simon:** Investigation, Writing - Review & Editing. **Lindsay P. Keller:** Resources, Investigation, Writing - Review & Editing, Supervision, Funding acquisition.

Acknowledgements

This study was supported in part by NASA grants 80NSSC21K1558 (JH) and 80NSSC20K0759 (MCL); KOPRI grant PE24050 (CP); and the JSC Coordinated Analysis Work Package (LPK) funded by the NASA Internal Scientist Funding Model. We gratefully acknowledge the access to the Electron Microbeam Analysis Labs at NASA JSC, the Electron Microprobe lab at KOPRI, and the UCLA ims-1290 ion microprobe facility that is partially supported by a grant from the NSF Instrumentation and Facilities program. The EPMA work at KOPRI by H. Kim is appreciated.

Appendix A. Supplementary material

The supplementary figures associated with this article contain SEM BSE images showing the locations of FIB sections and SIMS spots from the CAI *Big Guy*. A comparison of oxygen isotope data obtained from the UCLA ims-1290 ion microprobe and the NASA JSC NanoSIMS are also provided. The supplementary tables contain a complete dataset obtained using EPMA of individual minerals in the CAI *Big Guy*.

Data availability

Data are available through University of Houston Dataverse Repository at https://doi.org/10.18738/T8/WTXDGI.

References

Abreu N. M. and Brearley A. J. (2011) Deciphering the nebular and asteroidal record of silicates and organic material in the matrix of the reduced CV3 chondrite Vigarano. Meteorit. Planet. Sci. 46, 252–274.

Aléon J., El Goresy A. and Zinner E. (2007) Oxygen isotope heterogeneities in the earliest protosolar gas recorded in a meteoritic calcium–aluminum-rich inclusion. Earth Planet. Sci. Lett. 263, 114–127.

Aléon J. (2016) Oxygen isotopes in the early protoplanetary disk inferred from pyroxene in a classical type B CAI. Earth Planet. Sci. Lett. 440, 62–70.

Beckett J. R. and Stolper E. (1994) The stability of hibonite, melilite, and other aluminous phases in silicate melts: Implications for the origin of hibonite-bearing inclusions from carbonaceous chondrites. Meteoritics 29, 41–65.

Bonal L., Quirico E., Bourot-Denise M. and Montagnac G. (2006) Determination of the petrologic type of CV3 chondrites by Raman spectroscopy of included organic matter. Geochim. Cosmochim. Acta 70, 1849–1863.

Boss A. P., Alexander C. M. O'D. and Podolak M. (2012) Cosmochemical consequences of particle trajectories during FU Orionis outbursts by the early Sun. Earth Planet. Sci. Lett. 345–348, 18–26.

Brearley A. J. (1990) Carbon-rich aggregates in type 3 ordinary chondrites: Characterization, origins, and thermal history. Geochim. Cosmochim. Acta 54, 831–850.

Brearley A. J. and Krot A. N. (2013) Metasomatism in the early solar system: The record from chondritic meteorites. In Metasomatism and the Chemical Transformation of Rock (eds. D. E. Harlov and A. Austrheim). Springer, Berlin Heidelberg, pp. 659–789.

Bullock E. S., Knight K. B., Richter F. M., Kita N. T., Ushikubo T., MacPherson G. J., Davis A. M. and Mendybaev R. A. (2013) Mg and Si isotopic fractionation patterns in types B1 and B2 CAIs: Implications for formation under different nebular conditions. Meteorit. Planet. Sci. 48, 1440–1458.

Busemann H., Alexander M. O. D. and Nittler L. R. (2007) Characterization of insoluble organic matter in primitive meteorites by microRaman spectroscopy. Meteorit. Planet. Sci. 42, 1387–1416.

Ciesla F. J. (2010) The distributions and ages of refractory objects in the solar nebula. Icarus 208,

455–467.

Connelly J. N., Bizzarro M., Krot A. N., Nordlund Å., Wielandt D. and Ivanova M. A. (2012) The absolute chronology and thermal processing of solids in the solar protoplanetary disk. Science 338, 651–655.

Elphick S. C., Graham C. M. and Dennis P. F. (1988) An ion microprobe study of anhydrous oxygen diffusion in anorthite: a comparison with hydrothermal data and some geological implications. Contrib. Mineral. Petrol. 100, 490–495.

Fagan T. J., Krot A. N., Keil K. and Yurimoto H. (2004) Oxygen isotopic alteration in Ca-Al-rich inclusions from Efremovka: Nebular or parent body setting? Meteorit. Planet. Sci. 39, 1257–1272.

Freer W. and O'Reilly R. (1980) The diffusion of Fe^{2+} ions in spinels with relevance to the process of maghemitization. Miner. Mag. 43, 889–899.

Giletti B. J., Semet M. P. and Yund R. A. (1978) Studies in diffusion—III. Oxygen in feldspars: An ion microprobe determination. Geochim. Cosmochim. Acta 42, 45–57.

Grossman L. (1972) Condensation in the primitive solar nebula. Geochim. Cosmochim. Acta 36, 597–619.

Grossman L., Ebel D. S. and Simon S. B. (2002) Formation of refractory inclusions by evaporation of condensate precursors. Geochim. Cosmochim. Acta 66, 145–161.

Han J., Keller L. P., Liu M.-C., Needham A.W., Hertwig A. T., Messenger S. and Simon J. I. (2020) A coordinated microstructural and isotopic study of a Wark-Lovering rim on a Vigarano CAI. Geochim. Cosmochim. Acta 269, 639–660.

Ichimura S., Seto Y. and Tomeoka K. (2017) Nepheline formation in chondrite parent bodies: Verification through experiments. Geochim. Cosmochim. Acta 210, 114–131.

Ito M. and Ganguly J. (2009) Mg diffusion in minerals in CAIs: New experimental data for melilites and implications for the Al-Mg chronometer and thermal history of CAIs. Lunar and Planetary Science Conference, abstract 1753.

Jacobsen B., Yin Q.-Z., Moynier F., Amelin Y., Krot A. N., Nagashima K., Hutcheon I. D. and Palm H. (2008) ^{26}Al–^{26}Mg and ^{207}Pb–^{206}Pb systematics of Allende CAIs: Canonical solar initial $^{26}Al/^{27}Al$ ratio reinstated. Earth Planet. Sci. Lett. 272, 353–364.

Kamibayashi M., Tachibana S., Yamamoto D., Kawasaki N. and Yurimoto H. (2021) Effect of hydrogen gas pressure on calcium–aluminum-rich inclusion formation in the protosolar

disk: A laboratory simulation of open-system melt crystallization. Astrophys. J. Lett. 923, L12.

Katayama J., Itoh S. and Yurimoto H. (2012) Oxygen isotopic zoning of reversely zoned melilite crystals in a Fluffy Type A Ca-Al-rich inclusion from the Vigarano meteorite. Meteorit. Planet. Sci. 47, 2094–2106.

Kawasaki N., Simon S. B., Grossman L., Sakamoto N. and Yurimoto H. (2018) Crystal growth and disequilibrium distribution of oxygen isotopes in an igneous Ca-Al-rich inclusion from the Allende carbonaceous chondrite. Geochim. Cosmochim. Acta 221, 318–341.

Kawasaki N., Itoh S., Sakamoto N., Simon S. B., Yamamoto D. and Yurimoto H. (2021) Oxygen and Al-Mg isotopic constraints on cooling rate and age of partial melting of an Allende Type B CAI, Golfball. Meteorit. Planet. Sci. 56, 1224–1239.

Kita N. T., Ushikubo T., Knight K. B., Mendybaev R. A., Davis A. M., Richter F. M. and Fournelle J. H. (2012) Internal ^{26}Al-^{26}Mg isotope systematics of a Type B CAI: Remelting of refractory precursor solids. Geochim. Cosmochim. Acta 86, 37–51.

Krot A. N., Nagashima K., Fintor K. and Pál-Molnár E. (2019) Evidence for oxygen-isotope exchange in refractory inclusions from Kaba (CV3.1) carbonaceous chondrite during fluid-rock interaction on the CV parent asteroid. Geochim. Cosmochim. Acta 246, 419–435.

Krot A. N., Petaev M. I. and Nagashima K. (2021) Infiltration metasomatism of the Allende coarse-grained calcium-aluminum-rich inclusions. Prog. Earth Planet. Sci. 8, 61.

Krot A. N., Nagashima K., MacPherson G. J. and Ulyanov A. A. (2022) On the nature of oxygen-isotope heterogeneity of igneous calcium-aluminum-rich inclusions in CV carbonaceous chondrites. Geochim. Cosmochim. Acta 332, 327–354.

Lee M. R., Hutchison R. and Graham A. (1996) Aqueous alteration in the matrix of the Vigarano (CV3) carbonaceous chondrite. Meteorit. Planet. Sci. 31, 477–483.

Liu M.-C., Han J., Brearley A. J. and Hertwig A. T. (2019) Aluminum-26 chronology of dust coagulation and early solar system evolution. Sci. Adv. 5, eaaw3350.

Liermann H.-P. and Ganguly J. (2002) Diffusion kinetics of Fe^{2+} and Mg in aluminous spinel: Experimental determination and applications. Geochim. Cosmochim. Acta 66, 2903–2913.

MacPherson G. J. (2014) Calcium-aluminum-rich inclusions in chondritic meteorites. In: Treatise on Geochemistry Second Edition Volume 1 Meteorites and Cosmochemical Processes (ed. A. M. Davis). Elsevier, Oxford, pp. 201–246.

MacPherson G. J. and Grossman L. (1981) A once-molten, coarse-grained, Ca-rich inclusion in Allende. Earth Planet. Sci. Lett. 52, 16–24.

MacPherson G. J., Kita N. T., Ushikubo T., Bullock E. S. and Davis A. M. (2012) Well-resolved variations in the formation ages for Ca–Al-rich inclusions in the early Solar System. Earth Planet. Sci. Lett. 331–332, 43–54.

MacPherson G. J., Bullock E. S., Tenner T. J., Nakashima D., Kita N. T., Ivanova M. A., Krot A. N., Petaev M. I. and Jacobsen S. B. (2017) High precision Al-Mg systematics of forsterite-bearing Type B CAIs from CV3 chondrites. Geochim. Cosmochim. Acta 201, 65–82.

MacPherson G. J., Defouilloy C. and Kita N. T. (2018) High-precision Al–Mg isotopic systematics in USNM3898– The benchmark "ALL" for initial $^{87}Sr/^{86}Sr$ in the earliest Solar System. Earth Planet. Sci. Lett. 491, 238–243.

MacPherson G. J., Krot A. N., Kita N. T., Bullock E. S., Nagashima K., Ushikubo T. and Ivanova M. A. (2022) The formation of Type B CAIs: Evolution from Type A CAIs. Geochim. Cosmochim. Acta 321, 343–374.

Mendybaev R. A., Richter F. M. and Davis A. M. (2006) Crystallization of melilite from CMAS-liquids and the formation of the melilite mantle of Type B1 CAIs: experimental simulations. Geochim. Cosmochim. Acta 70, 2622–2642.

Morioka M. and Nagasawa H. (1991) Diffusion in single crystals of melilite: II. Cations. Geochim. Cosmochim. Acta 55, 751–759.

Nomura K. and Miyamoto M. (1998) Hydrothermal experiments on alteration of Ca–Al-rich inclusions (CAIs) in carbonaceous chondrites: Implication for aqueous alteration in parent asteroids. Geochim. Cosmochim. Acta 62, 3575–3588.

Norris T. L., Gancarz A. J., Rokop D. J. and Thomas K. W. (1983) Half-life of ^{26}Al. J. Geophys. Res. 88, B331–B333.

Oishi Y., Terai R. and Ueda H. (1974) Oxygen diffusion in liquid silicates and relation to their viscosity. In Mass Transport in Ceramics (eds. A. R. Cooper and A. H. Heuer). Premium Press, pp. 297–310.

Park C., Wakaki S., Sakamoto N., Kobayashi S. and Yurimoto H. (2012) Oxygen isotopic composition of the solar nebula gas inferred from high-precision isotope imaging of melilite crystals in an Allende CAI. Meteorit. Planet. Sci. 47, 2070–2083.

Paque J. M., Beckett J. R., Ishii H. A., Aléon-Toppani A., Burnett D. S., Teslich N., Dai Z. R. and

Bradley J. P. (2009) The formation of boundary clinopyroxenes and associated glass veins in type B1 CAIs. Meteorit. Planet. Sci. 44, 665–687.

Richter F. M., Janney P. E., Mendybaev R. A., Davis A. M. and Wadhwa M. (2007) Elemental and isotopic fractionation of Type B CAI-like liquids by evaporation. Geochim. Cosmochim. Acta 71, 5544–5564.

Ryerson F. J. and McKeegan K. D. (1994) Determination of oxygen self-diffusion in åkermanite, anorthite, diopside, and spinel: Implications for oxygen isotopic anomalies and the thermal histories of Ca–Al-rich inclusions. Geochim. Cosmochim. Acta 58, 3713–3734.

Simon J. I. and Young E. D. (2011) Resetting, errorchrons and the meaning of canonical CAI initial $^{26}Al/^{27}Al$ values. Earth Planet. Sci. Lett. 304, 468–482.

Simon J. I., Young E. D., Russell S. S., Tonui E. K., Dyl K. A. and Manning C. E. (2005) A short timescale for changing oxygen fugacity in the solar nebula revealed by high-resolution ^{26}Al–^{26}Mg dating of CAI rims. Earth Planet. Sci. Lett. 238, 272–283.

Simon J. I., Hutcheon I. D., Simon S. B., Matzel J. E. P., Ramon E. C., Weber P. K., Grossman L. and DePaolo D. J. (2011) Oxygen isotope variations at the margin of a CAI records circulation within the solar nebula. Science 331, 1175–1178.

Simon J. I., Matzel J. E. P., Simon S. B., Hutcheon I. D., Ross D. K., Weber P. K. and Grossman L. (2016) Oxygen isotopic variations in the outer margins and Wark–Lovering rims of refractory inclusions. Geochim. Cosmochim. Acta 186, 242–276.

Simon J. I., Ross D. K., Nguyen A. N., Simon S. B. and Messenger S. (2019) Molecular cloud origin for oxygen isotopic heterogeneity recorded by a primordial spinel-rich refractory inclusion. Astrophys. J. Lett. 884, L29.

Simon S. B. and Grossman L. (2004) A preferred method for the determination of bulk compositions of coarse-grained refractory inclusions and some implications of the results. Geochim. Cosmochim. Acta 68, 4237–4248.

Simon S. B. and Grossman L. (2006) A comparative study of melilite and fassaite in Type B1 and B2 refractory inclusions. Geochim. Cosmochim. Acta 70, 7780–7798.

Simon S. B., Davis A. M. and Grossman L. (1999) Origin of compact Type A refractory inclusions from CV3 carbonaceous chondrites. Geochim. Cosmochim. Acta 63, 1233–1248.

Stolper E. (1982) Crystallization sequences of Ca–Al-rich inclusions from Allende: An experimental study. Geochim. Cosmochim. Acta 46, 2159–2180.

785 Stolper E. and Paque J. M. (1986) Crystallization sequences of Ca–Al-rich inclusions from Allende:
786 The effects of cooling rate and maximum temperature. Geochim. Cosmochim. Acta 50,
787 1785–1806.
788 Suzumura A., Kawasaki N., Seto Y., Yurimoto H. and Itoh S. (2021) Origin of minerals in
789 åkermanite-rich patch texture and oxygen isotopic evolution of compact Type A Ca-Al-
790 rich inclusions from the Northwest Africa 7865 CV chondrite. Geochim. Cosmochim. Acta
791 303, 51–65.
792 Van Orman J. A., Cherniak D. J. and Kita N. T. (2014) Magnesium diffusion in plagioclase:
793 Dependence on composition, and implications for thermal resetting of the ^{26}Al–^{26}Mg early
794 solar system chronometer. Earth Planet. Sci. Lett. 385, 79–88.
795 Wark D. A. and Boynton W. V. (2001) The formation of rims on calcium–aluminum-rich
796 inclusions: Step I Flash heating. Meteorit. Planet. Sci. 36, 1135–1166.
797 Wark D. A. and Lovering J. F. (1982) Evolution of Ca–Al-rich bodies in the earliest solar system:
798 Growth by incorporation. Geochim. Cosmochim. Acta 46, 2595–2607.
799 Yamamoto D., Kawasaki N., Tachibana S., Kamibayashi M. and Yurimoto H. (2021) An
800 experimental study on oxygen isotope exchange reaction between CAI melt and low-
801 pressure water vapor under simulated solar nebular conditions. Geochim. Cosmochim.
802 Acta 314, 108–120.
803 Yamamoto D., Kawasaki N., Tachibana S., Kamibayashi M. and Yurimoto H. (2022) Oxygen
804 isotope exchange kinetics between CAI melt and carbon monoxide gas: Implication for
805 CAI formation in the earliest Solar System. Geochim. Cosmochim. Acta 336, 104–112.
806 Yoshitake M., Koide Y. and Yurimoto H. (2005) Correlations between oxygen-isotopic
807 composition and petrologic setting in a coarse-grained Ca, Al–rich inclusion. Geochim.
808 Cosmochim. Acta 69, 2663–2674.
809 Young E. D., Simon J. I., Galy A., Russell S. S., Tonui E. and Lovera O. (2005) Supra-canonical
810 ^{26}Al/^{27}Al and the residence time of CAIs in the solar protoplanetary disk. Science 308,
811 223–227.
812 Yurimoto H., Morioka M. and Nagasawa H. (1989) Diffusion in single crystals of melilite: I.
813 Oxygen. Geochim. Cosmochim. Acta 53, 2387–2394.
814 Yurimoto H., Nagasawa H., Mori Y. and Matsubaya O. (1994) Micro-distribution of oxygen
815 isotopes in a refractory inclusion from the Allende meteorite. Earth Planet. Sci. Lett. 128,

816 47–53.
817 Yurimoto H., Ito M. and Nagasawa H. (1998) Oxygen isotope exchange between refractory
818 inclusion in Allende and solar nebula gas. Science 282, 1874–1877.
819 Zhang X., Ganguly J. and Ito M. (2010) Ca-Mg diffusion in diopside: tracer and chemical inter-
820 diffusion coefficients. Contrib. Miner. Petrol. 159, 175–186.

TABLES

Table 1. Oxygen isotopic compositions of individual minerals from the CAI *Big Guy*.

mineral	spot #	$\delta^{18}O$	2σ	$\delta^{17}O$	2σ	$\Delta^{17}O$	2σ	TiO_2^{av} (wt%)	$Åk^{av}$ (mol%)
Core									
spinel	S1	−46.9	0.8	−48.4	1.0	−24.0	0.9		
	S2	−46.6	0.8	−47.7	1.0	−23.5	0.9		
Al,Ti-diopside	F2	−9.7	0.8	−16.5	1.0	−11.4	0.9	16.2	
	F3	−10.0	0.8	−18.2	1.0	−13.0	0.9	16.0	
	F4	−24.2	0.8	−29.7	1.0	−17.1	0.9	13.1	
	F5	−8.6	0.8	−16.1	1.0	−11.7	0.9	15.6	
	F6	−28.8	0.8	−33.3	1.0	−18.3	0.9	11.2	
Mantle									
spinel	S3	−46.1	0.8	−49.4	1.0	−25.4	0.9		
	S4	−47.9	0.8	−47.9	1.0	−23.0	0.9		
melilite	M1	−11.3	0.8	−13.3	1.0	−7.4	0.9		11.4
	Grain #1								
	M8	−2.1	0.8	−10.3	0.5	−8.7	0.5		30.8
	M9	−3.8	0.8	−12.0	0.5	−9.5	0.5		15.8
	M10	−10.9	0.8	−18.5	0.5	−12.3	0.5		12.1
	M11	−20.5	0.8	−26.2	0.5	−15.1	0.5		13.1
	M12	−21.0	0.8	−26.9	0.5	−15.5	0.5		10.5
	M13	−12.3	0.8	−20.1	0.5	−13.2	0.5		9.2
	Grain #2								
	M2	−20.5	0.8	−20.8	1.0	−10.1	0.9		5.5
	M3	−28.6	0.8	−30.0	1.0	−15.1	0.9		10.6
	M4	−21.2	0.8	−21.9	1.0	−10.8	0.9		8.5
	M5	−10.3	0.8	−12.5	1.0	−7.2	0.9		54.4
	M6	−9.6	0.8	−10.5	1.0	−5.6	0.9		53.6
	M7	−10.4	0.8	−11.8	1.0	−6.4	0.9		55.5
	M14	10.6	0.8	1.7	0.5	−3.3	0.5		55.4
	M15	4.4	0.8	−5.0	0.5	−6.8	0.5		47.9
	M16	4.0	0.8	−5.0	0.5	−6.6	0.5		33.8
	M17	−1.1	0.8	−9.2	0.5	−8.1	0.5		19.1
	M18	−18.0	0.8	−24.6	0.5	−14.8	0.5		14.3
	M19	−16.8	0.8	−23.8	0.5	−14.5	0.5		12.4
	M20	−19.9	0.8	−26.2	0.5	−15.3	0.5		11.4
WL rim									
spinel	S5	−47.1	0.8	−49.6	1.0	−25.2	0.9		
diopside	D1	−38.5	0.8	−43.0	1.0	−23.0	0.9	0.9	

* Spots M8 to M20 were obtained from the first session (3O-I), whereas the rest was obtained from the second session (3O-II). TiO_2^{av} (wt%) and $Åk^{av}$ (mol%) are average values of multiple EPMA analyses around SIMS pits of Al,Ti-diopside, melilite, and diopside.

828 **Table 2.** Al-Mg isotopic compositions of individual minerals from the CAI *Big Guy*.

mineral	spot #	δ^{25}Mg (‰)	2σ	^{27}Al/^{24}Mg	2σ	Δ^{26}Mg* (‰)	2σ
Core							
spinel	S11	10.78	0.17	2.56	0.01	0.96	0.10
	S12	10.54	0.18	2.57	0.01	0.81	0.10
Al,Ti-diopside	F11	9.42	0.27	2.23	0.00	0.91	0.23
Mantle							
melilite	M21	8.26	0.20	2.75	0.02	1.19	0.30
	M22	8.15	0.21	5.02	0.05	1.80	0.31
	M23	8.16	0.27	13.94	0.08	5.00	0.57
	M24	7.62	0.18	13.32	0.08	5.00	0.30
	M25	7.82	0.27	14.39	0.09	4.85	0.56
	M26	7.21	0.27	12.93	0.12	5.69	0.34
	M27	7.69	0.22	7.78	0.04	2.91	0.39
	M28	7.80	0.47	17.31	0.49	5.61	0.70
	M29	8.02	0.28	19.33	0.04	7.11	0.51
	M30	8.21	0.14	4.19	0.02	1.43	0.25
	M31	7.91	0.33	15.68	0.11	5.60	0.61
	M32	7.72	0.20	15.75	0.07	5.08	0.34
	M33	7.86	0.31	15.59	0.09	4.58	0.48
	M34	7.71	0.27	19.49	0.05	6.37	0.49
	M35	6.53	0.42	21.07	0.36	6.94	1.22
	M36	6.84	0.23	12.45	0.11	4.79	0.44
	M37	8.29	0.12	2.12	0.04	0.91	0.21
	M38	8.24	0.13	2.76	0.02	0.80	0.19
	M39	8.39	0.15	2.51	0.02	0.73	0.21
	M40	8.01	0.12	4.83	0.02	1.72	0.28
	M41	7.94	0.16	4.94	0.04	1.53	0.28
	M42	7.62	0.29	11.08	0.08	3.97	0.58

829

FIGURE CAPTIONS

Figure 1. (a) BSE image and (b) corresponding combined elemental map in Mg (red), Ca (green), and Al (blue) Kα x-rays of the CAI *Big Guy*. The CAI shows a distinct core-mantle-rim structure. The dotted line A-B indicates an electron microprobe traverse across a single melilite crystal shown in Figure 3b. Abbreviations hereafter: sp = spinel; mel = melilite; AlTi-di = Al,Ti-rich diopside; WL = Wark-Lovering rim; AR = olivine-rich accretionary rim.

Figure 2. (a, d, f) BSE images, (b, e, g) combined elemental maps in Mg (red), Ti (green), and Al (blue) Kα x-rays, and (c) Fe Kα x-ray map of the core region of the CAI *Big Guy*. Abbreviations hereafter: pv = perovskite.

Figure 3. Chemical compositions of Al,Ti-diopside and melilite from the CAI *Big Guy*. (a) A plot of TiO_2 versus Al_2O_3 contents in Al,Ti-diopside from the CAI core. (b) Compositional profile across a single melilite grain in the CAI mantle. The electron microprobe traverse, as indicated by the A-B line in Figure 1, was obtained along the elongation direction of the melilite crystal with a spacing of 2 μm between points.

Figure 4. (a) BF STEM image and (b) compositional profile of Al,Ti-diopside along the core edge that is rimmed by a thin layer of Al-diopside. The solid line in (a) indicates the TEM EDX traverse across the grain boundary, with 0 being the start point. The vertical dotted line in (b) represents the grain boundary between two chemically different diopsides. Abbreviations hereafter: Al-di = Al-rich diopside; alt = secondary alteration phase.

Figure 5. (a) BF STEM image of perovskite grains in the symplectic intergrowth with Al,Ti-diopside and melilite along the core-mantle boundary. (b, c) BF STEM and HRTEM images of a secondary Fe-rich vein associated with melilite grains along the core-mantle boundary. Some veins between melilite grains are zoned, with a denser and more Fe-rich middle. The veins are poorly crystalline and contains phyllosilicates exhibiting the 0.7 nm basal spacing of serpentine, as indicated by two parallel lines in (c).

Figure 6. Oxygen isotopic compositions of Al,Ti-diopside and melilite from the CAI *Big Guy*. (a) A relationship between $\Delta^{17}O$ value and TiO_2 content of diopside. (b) A relationship between $\Delta^{17}O$ value and åkermanite content of melilite. (c) A distribution of $\Delta^{17}O$ values on the TiO_2 content map of the core Al,Ti-diopside. (d) A distribution of $\Delta^{17}O$ values on the åkermanite content map of the mantle melilite. Terrestrial fractionation (TF) line is shown for reference. Our SIMS data are compared with those obtained from CTA and B1 CAIs, which were reported in Aléon et al. (2007), Aléon (2016), Kawasaki et al. (2018), and Suzumura et al. (2021).

Figure 7. Magnesium isotopic compositions of individual minerals from the CAI *Big Guy*. A dotted line represents the CAI's isochron with $(^{26}Al/^{27}Al)_0 = (4.93\pm0.18)\times10^{-5}$ and $\Delta^{26}Mg_0^* = -0.01\pm0.1‰$ (2σ).

Figure 8. Arrhenius plots of oxygen and Mg diffusivities in spinel, melilite, anorthite, and diopside. Oxygen diffusion in anorthite was compared under both dry and wet conditions, and a dry condition was considered for oxygen diffusion in all other minerals, as well as Mg diffusion in all minerals. Oxygen and Mg diffusivities are indicated by dashed and solid lines, respectively. Vertical solid lines indicate temperature ranges estimated for (a) fluid-assisted thermal metamorphism on the parent body and (b) gas-solid interaction in the solar nebula. Diffusion data were from Gilletti et al. (1978), Yurimoto et al. (1989), Morioka and Nagasawa (1991), Ryerson and McKeegan (1994), Liermann and Ganguly (2002), Ito and Ganguly (2009), Zhang et al. (2010), and Van Orman et al. (2014).

Figure 9. Oxygen diffusion in anorthite under dry and wet conditions at 300–400℃, estimated for a temperature range of peak metamorphic heating on the Vigarano parent body. The preservation of ^{16}O-rich composition of fine-grained anorthite (typically <5 μm in size) in the WL rim constrains peak metamorphic heating to have occurred for less than 50 years.

Figure 10. Oxygen and Mg diffusion time and length for spinel, melilite, and diopside below the solidus temperature of melilite at 1100℃ (a) and 1400℃ (b). Oxygen and Mg diffusion data are indicated by dashed and solid lines, respectively.

FIGURES

Figure 1. (a) BSE image and (b) corresponding combined elemental map in Mg (red), Ca (green), and Al (blue) Kα x-rays of the CAI *Big Guy*. The CAI shows a distinct core-mantle-rim structure. The dotted line A-B indicates an electron microprobe traverse across a single melilite crystal shown in Figure 3b. Abbreviations hereafter: sp = spinel; mel = melilite; AlTi-di = Al,Ti-rich diopside; WL = Wark-Lovering rim; AR = olivine-rich accretionary rim.

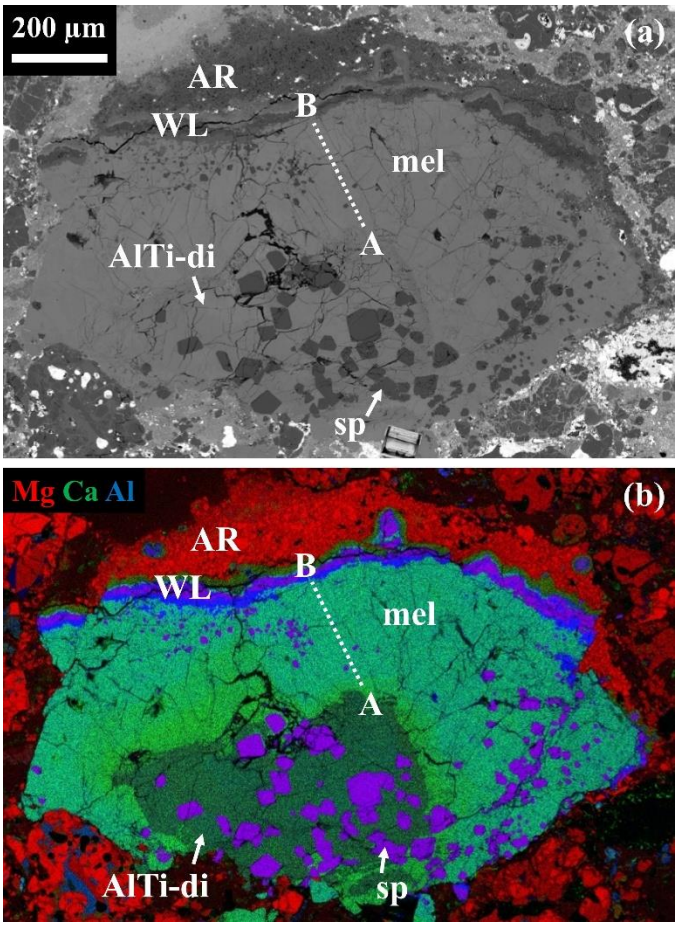

Figure 2. (a, d, f) BSE images, (b, e, g) combined elemental maps in Mg (red), Ti (green), and Al (blue) Kα x-rays, and (c) Fe Kα x-ray map of the core region of the CAI *Big Guy*. Abbreviations hereafter: pv = perovskite.

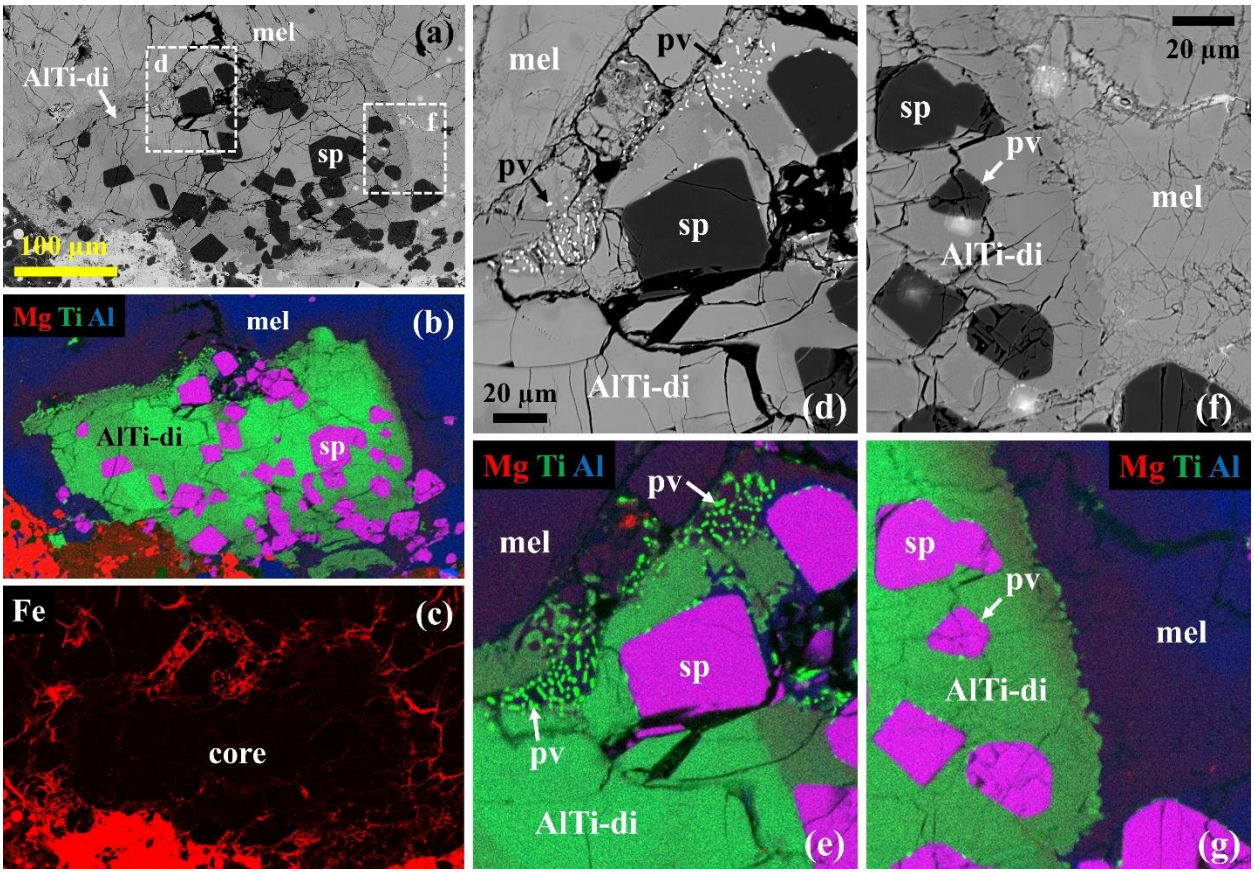

Figure 3. Chemical compositions of Al,Ti-diopside and melilite from the CAI *Big Guy*. (a) A plot of TiO_2 versus Al_2O_3 contents in Al,Ti-diopside from the CAI core. (b) Compositional profile across a single melilite grain in the CAI mantle. The electron microprobe traverse, as indicated by the A-B line in Figure 1, was obtained along the elongation direction of the melilite crystal with a spacing of 2 μm between points.

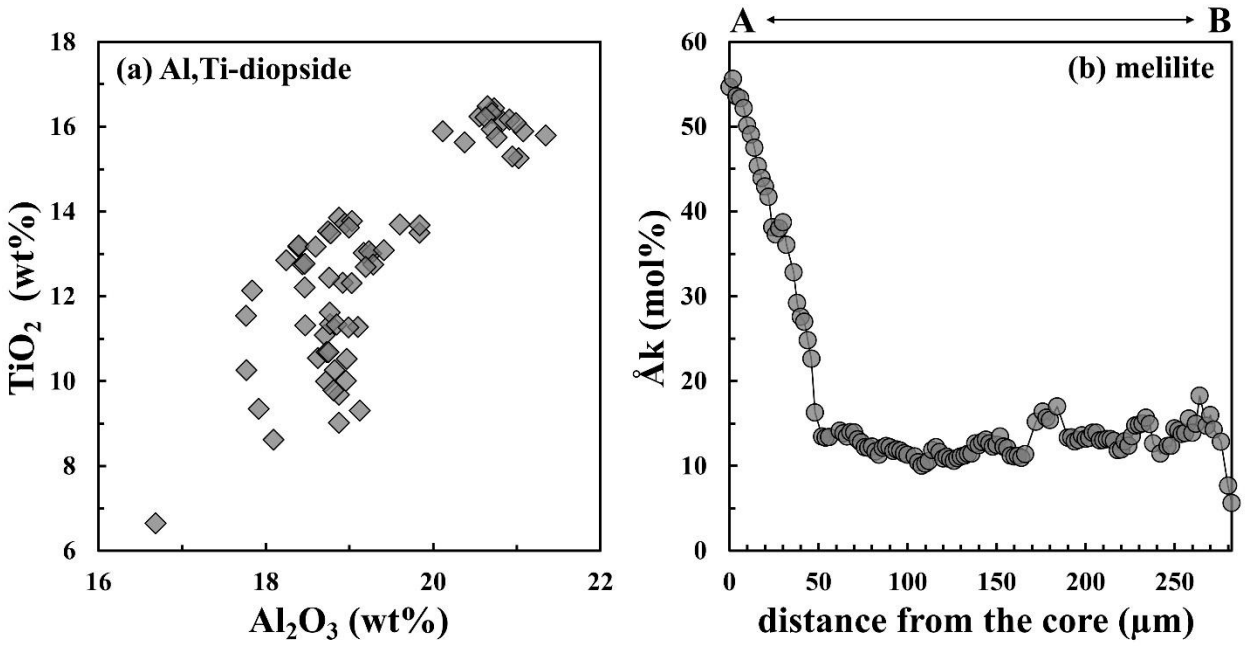

Figure 4. (a) BF STEM image and (b) compositional profile of Al,Ti-diopside along the core edge that is rimmed by a thin layer of Al-diopside. The solid line in (a) indicates the TEM EDX traverse across the grain boundary, with 0 being the start point. The vertical dotted line in (b) represents the grain boundary between two chemically different diopsides. Abbreviations hereafter: Al-di = Al-rich diopside; alt = secondary alteration phase.

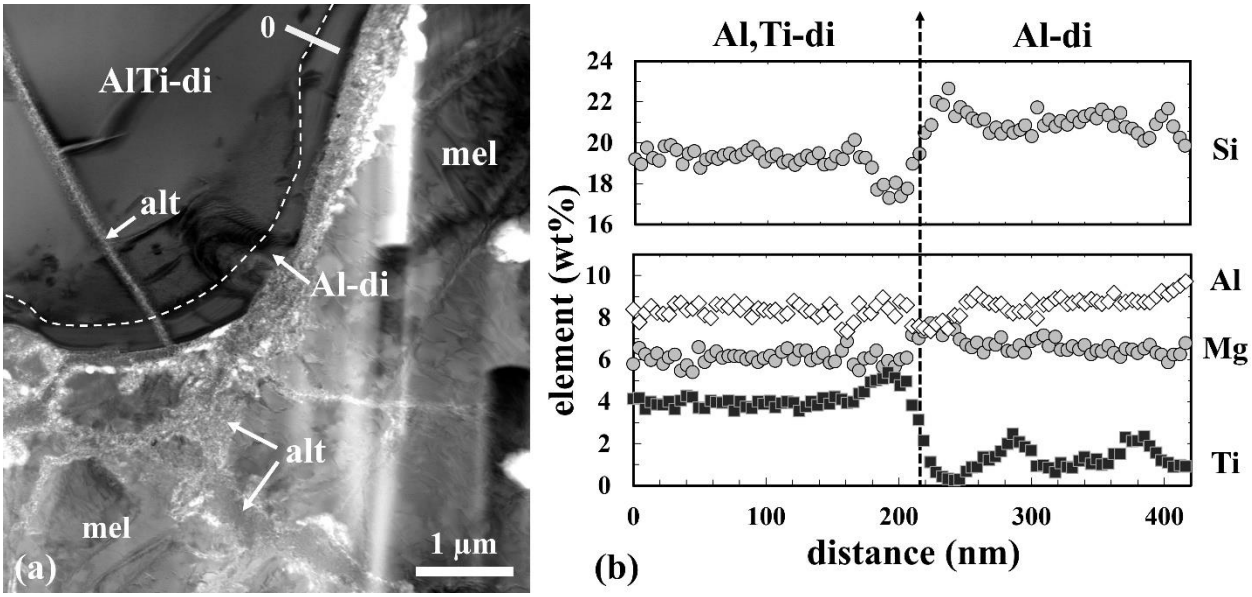

Figure 5. (a) BF STEM image of perovskite grains in the symplectic intergrowth with Al,Ti-diopside and melilite along the core-mantle boundary. (b, c) BF STEM and HRTEM images of a secondary Fe-rich vein associated with melilite grains along the core-mantle boundary. Some veins between melilite grains are zoned, with a denser and more Fe-rich middle. The veins are poorly crystalline and contains phyllosilicates exhibiting the 0.7 nm basal spacing of serpentine, as indicated by two parallel lines in (c).

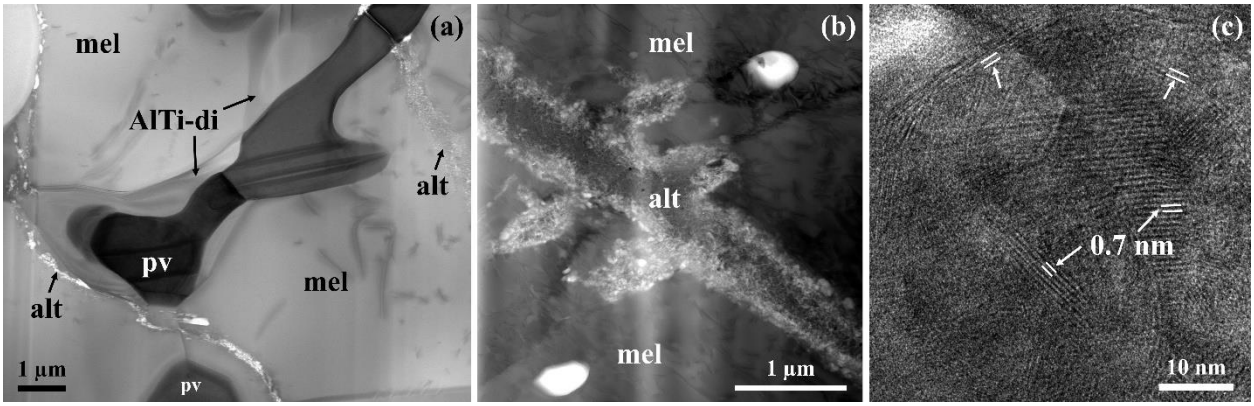

Figure 6. Oxygen isotopic compositions of Al,Ti-diopside and melilite from the CAI *Big Guy*. (a) A relationship between $\Delta^{17}O$ value and TiO_2 content of diopside. (b) A relationship between $\Delta^{17}O$ value and åkermanite content of melilite. (c) A distribution of $\Delta^{17}O$ values on the TiO_2 content map of the core Al,Ti-diopside. (d) A distribution of $\Delta^{17}O$ values on the åkermanite content map of the mantle melilite. Terrestrial fractionation (TF) line is shown for reference. Our SIMS data are compared with those obtained from CTA and B1 CAIs, which were reported in Aléon et al. (2007), Aléon (2016), Kawasaki et al. (2018), and Suzumura et al. (2021).

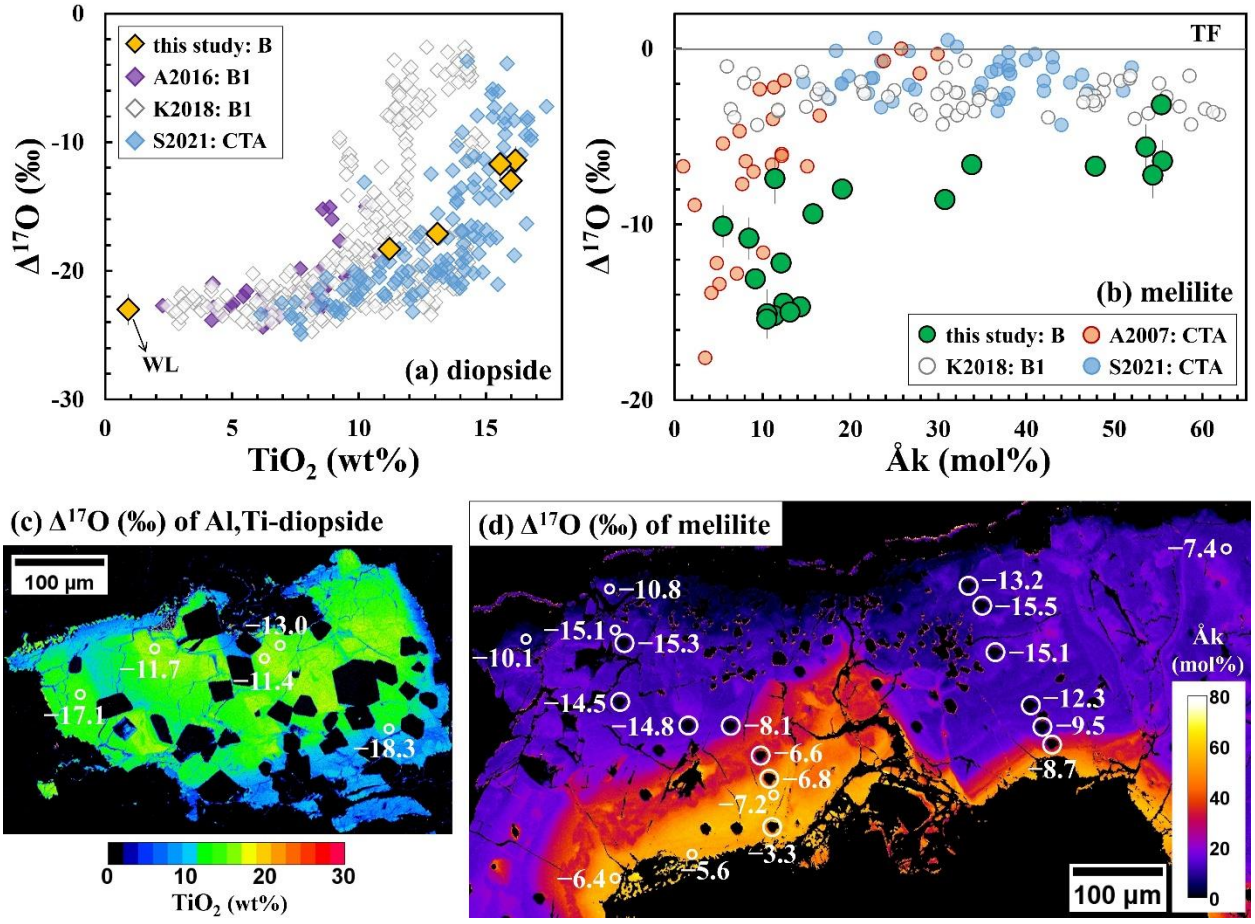

Figure 7. Magnesium isotopic compositions of individual minerals from the CAI *Big Guy*. A dotted line represents the CAI's isochron with $(^{26}Al/^{27}Al)_0 = (4.93\pm0.18)\times10^{-5}$ and $\Delta^{26}Mg_0^* = -0.01\pm0.1‰$ (2σ).

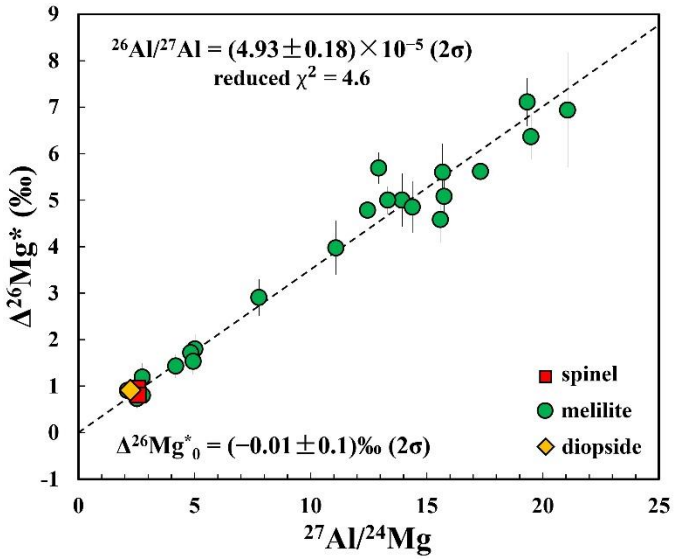

Figure 8. Arrhenius plots of oxygen and Mg diffusivities in spinel, melilite, anorthite, and diopside. Oxygen diffusion in anorthite was compared under both dry and wet conditions, and a dry condition was considered for oxygen diffusion in all other minerals, as well as Mg diffusion in all minerals. Oxygen and Mg diffusivities are indicated by dashed and solid lines, respectively. Vertical solid lines indicate temperature ranges estimated for (a) fluid-assisted thermal metamorphism on the parent body and (b) gas-solid interaction in the solar nebula. Diffusion data were from Gilletti et al. (1978), Yurimoto et al. (1989), Morioka and Nagasawa (1991), Ryerson and McKeegan (1994), Liermann and Ganguly (2002), Ito and Ganguly (2009), Zhang et al. (2010), and Van Orman et al. (2014).

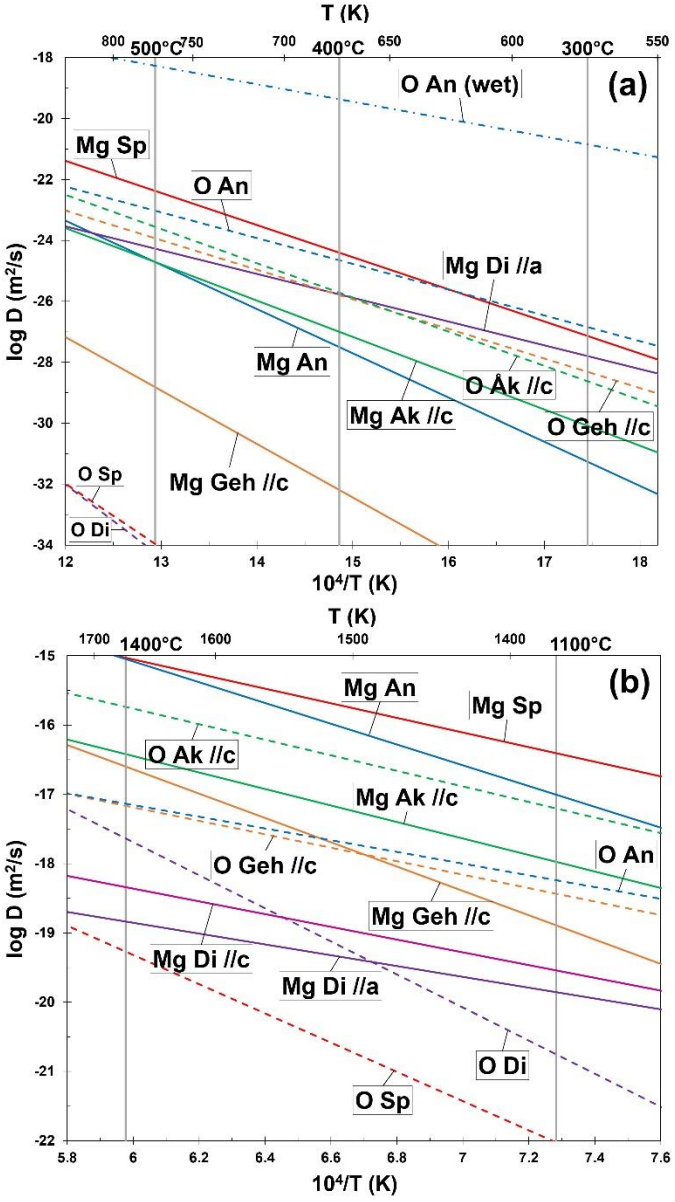

Figure 9. Oxygen diffusion in anorthite under dry and wet conditions at 300–400°C, estimated for a temperature range of peak metamorphic heating on the Vigarano parent body. The preservation of ^{16}O-rich composition of fine-grained anorthite (typically <5 μm in size) in the WL rim constrains peak metamorphic heating to have occurred for less than 50 years.

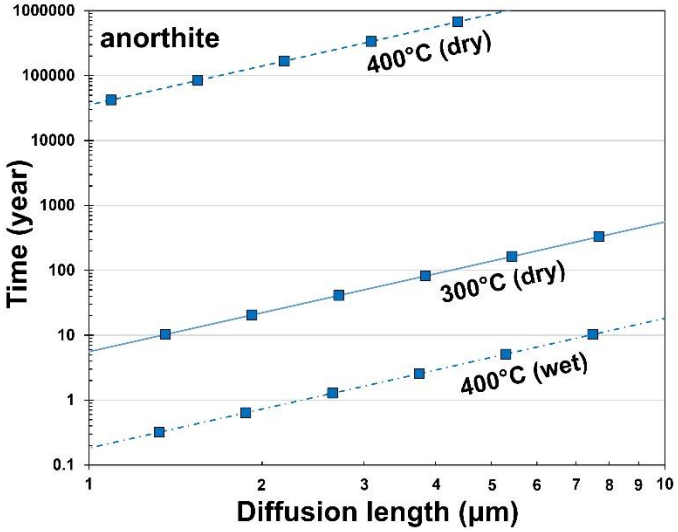

Figure 10. Oxygen and Mg diffusion time and length for spinel, melilite, and diopside below the solidus temperature of melilite at 1100℃ (a) and 1400℃ (b). Oxygen and Mg diffusion data are indicated by dashed and solid lines, respectively.

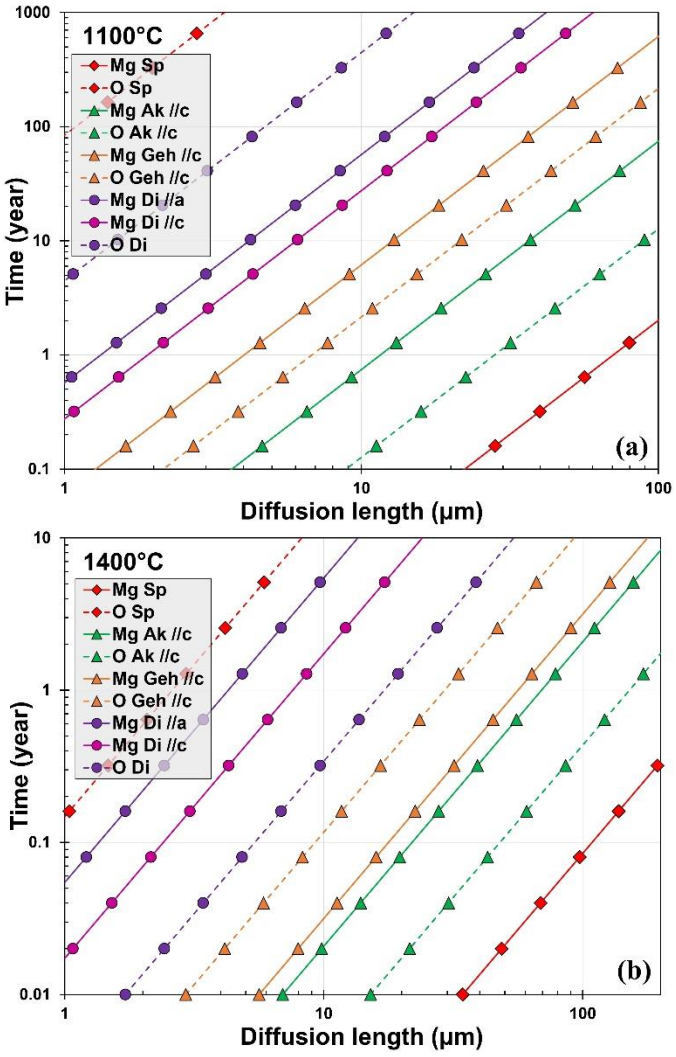

Declaration of interests

☒ **The authors declare that they have no known competing financial interests or personal relationships that could have appeared to influence the work reported in this paper.**

☐ The author is an Editorial Board Member/Editor-in-Chief/Associate Editor/Guest Editor for [Journal name] and was not involved in the editorial review or the decision to publish this article.

☐ The authors declare the following financial interests/personal relationships which may be considered as potential competing interests:

GCA Submission Checklist

Please complete this checklist by entering an "X" for each entry once you have verified that your manuscript complies with the requirement. In some cases, the requirement may not be applicable and "NA" should instead be entered. Please upload this form in Editorial Manager when you submit your manuscript. Before completing this checklist, please review the Guide for Authors: https://www.sciencedirect.com/journal/geochimica-et-cosmochimica-acta/publish/guide-for-authors

Please use Acrobat Reader or a similar program to complete this form. ***Do not use Preview on a Mac, it does not record entries correctly in PDF forms.***

X The title summarizes the major scientific finding of the study rather than the study location or the methods used. The title should not convey that the paper is a regional case study, which GCA does not publish, nor should it list the name of countries.

X The manuscript lists only one corresponding author.
X The first page of the manuscripts lists the names and affiliations of all authors. Affiliations are needed for identifying conflicts of interests in the review process. ***Note that manuscripts lacking author affiliation information on the first page will be returned without review.***

X The abstract is less than 500 words in length and formatted as 1 to 2 paragraphs.
X Citation of references in the abstract have been avoided to the extent possible.
X Acronyms/abbreviations have only been defined in the abstract if the term appears three or more times.

X Three or more keywords have been provided. ***Do not provide Highlights or Graphical Abstracts, these are not part of GCA format.***

X The introduction is a single section without subsections and avoids excessive review.

X The manuscript contains separate Results and Discussion sections. If this is not possible, then a request and justification for combined Results and Discussion sections have been added to the Cover Letter.
X The Discussion section (or a subsection) clearly addresses the broader geochemical and/or cosmochemical significance and implications of the study.

X The manuscript text is written with inclusive language, leaves out words or phrases that are slang or based on cultural elements not relevant to the study, and avoids the use of terms appropriated from non-dominant cultures.
X Acronyms/abbreviations are defined at first use in the main text. Note that the abstract is considered a separate document and all acronyms/abbreviations used in the main text must be defined in the main text.
X Equations have been submitted as editable text and not as images.

X All figures comply with the Artwork requirements listed in the Guide for Authors.
NA All maps appearing in the paper are based on physical geographic features and do not display national borders or other political boundaries. ***Maps may not display borders.***

X All tables intended for publication in the main paper have been provided in a format generated using Microsoft Word, LaTeX, or similar document preparation software. ***Tables are not accepted in XLSX format and cannot contain shading or color.***
X All numbers in tables appear in decimal format (e.g., 2.873), scientific notation (e.g., 4.76×10^{-5}), or a related format. Do not use Excel-style scientific notation (e.g., 8.54E-03).

X *(Required only if the paper involves meteorite samples)* Meteorite nomenclature uses the approved list of names in the Meteoritical Bulletin Database and new meteorite names have been submitted for consideration by the Meteorite Nomenclature Committee.

X The Acknowledgments identifies the source(s) of funding that supported the study.

NA Any use of generative AI in preparation of the manuscript is disclosed in the paper. See the Disclosure Instructions in the GCA Guide for Authors.

X The data underlying all figures and tables in the main paper and any supplementary material have been made available in a text-based numerical format via deposition in an open-access repository. A section entitled "Data Availability" has added followed by a sentence indicating the repository and the URL for the data. An example of this section might appear as follows:

Data Availability
Data are available through Mendeley Data at https://doi.org/10.17632/cfdzx2rh8z.1.

All data appearing as a point, line, or bar plot, including spectra, diffraction patterns, and chromatograms, must be provided. All data appearing in the manuscript and any supplementary documents, figures, or tables must be made available upon submission. Images, maps, movies, and similar large datasets are excluded from this requirement. Consult the Data Availability section of the Guide for Authors for more details on complying with this requirement. Note that failure to comply with this requirement may result in the manuscript being returned without review.

X If one or more Supplementary Material files are included in the submission, a section titled "Appendix A. Supplementary Material" is inserted between the Acknowledgements and References and briefly describes the contents of all supplementary files. This text should explain to readers the information that they can find in the supplementary file(s). This should be written in paragraph format, not as a list of captions. Do not discuss filenames, these names are lost when a paper is published online. Do not include text stating that the supplementary material can be found online, similar text is added during production. Note that this brief section in the main paper is the only use of the term "Appendix" in GCA. ***The supplementary files are NOT appendices, they are simply "Supplementary Material".***

X Supplementary figures and their captions are embedded in a single PDF document rather than uploaded as a series of separate image or PDF files.

X Supplementary files have been combined into a single PDF document to the extent possible. This file includes a cover page indicating the article title and authors. ***Note that DOCX files are not accepted as supplements; these must be converted to PDF before submission.***

X *(Required if manuscript was prepared in Microsoft Word or similar software)* The References are in a style generally similar to current GCA format. ***References should not be numbered.***

NA *(Required if manuscript was prepared in LaTeX)* The manuscript was prepared using the Elsevier article class in combination with BibTeX (use elsarticle-harv.bst), as described at: https://www.elsevier.com/authors/policies-and-guidelines/latex-instructions

X Citation of conference abstracts has been avoided. Exceptions may be made for older abstracts (generally pre-1990) that have long been cited by the community. For each citation of a conference abstract that authors wish to include, include an individual justification in the Cover Letter. Such citations must comply with the policies outlined in the Guide for Authors.

X Papers in preparation are not cited. Papers in review are either not cited or a full copy of the cited work is provided as Review-Only Material.